

Department of Physics and Astronomy
University of Heidelberg

Bachelor Thesis in Physics
submitted by

Maurice Donner

born in Aachen (Germany)

2021

Tracking Cosmic Muons with the ALICE Pixel Detector
A Study of
Monolithic Active Pixel Sensors
and
Telescope Alignment

This Bachelor Thesis has been carried out by Maurice Donner at the
Physikalisches Institut, University Heidelberg
under the supervision of
Prof. Dr. Silvia Masciocchi

Abstract

The upgrade of the ALICE Inner Tracking System (ITS) is being performed during the currently ongoing shutdown period (Long Shutdown 2 (LS2)) of the CERN Large Hadron Collider (LHC). The former ITS is replaced with seven concentric layers of Monolithic Active Pixel Sensors (MAPS) called the ALICE Pixel Detector (ALPIDE).

The scope of this thesis is to test a telescope of seven ALPIDE sensors operating as a cosmic particle detector, in order to study the behaviour of the telescope under unconventional conditions, and perform tracking and an alignment of the setup. The mode of operation for cosmic muon detection is presented and a particle tracking method is implemented in an attempt to achieve an accurate detector alignment based on relatively large angle cosmic muon tracks. For tracking, at least four of the seven available sensors are required to detect a hit. Two different iterative alignment procedures based on a reduced χ^2 -statistic are tested and compared. Estimations about particle rates, pixel cluster sizes, and detection efficiency are briefly presented. Finally, a very accurate alignment of the setup is reached, maximizing track quality and opening up the possibility for further analysis.

Zusammenfassung

Das Upgrade des hochauflösenden Inner Tracking System (ITS) wird derzeit am ALICE Experiment am CERN Large Hadron Collider (LHC) durchgeführt. Dabei werden die alten Sensoren mit sieben Monolithic Active Pixel Sensors (MAPS) Schichten, dem ALICE Pixel Detector (ALPIDE), ersetzt.

In dieser Arbeit wird ein Teleskop aus sieben ALPIDE Sensoren zur Detektion von kosmischen Muonen verwendet, um das Verhalten des Teleskops unter unkonventionellen Verhältnissen zu untersuchen, und eine präzise Ausrichtung des Detektors zu erlangen. Zuerst wird die Operation des Detektors beschrieben. Daraufhin wird eine Methode zur Rekonstruktion der Teilchentrajektorie implementiert. Diese Teilchenspuren (Tracks) werden verwendet, um eine präzise Ausrichtung der einzelnen Detektorschichten zu erreichen. Dazu werden Tracks verwendet, bei denen das Teilchen mindestens vier der sieben Sensoren getroffen hat. Zwei verschiedene Algorithmen, basierend auf einer reduzierten χ^2 -Statistik, werden für die Ausrichtung des Teleskops diskutiert, und verglichen. Des Weiteren werden kurz Schätzungen zur Teilchenrate, Größe von Pixelgruppen, und Sensoreffizienz präsentiert und mit den Messwerten verglichen. Schließlich wird eine hochpräzise Ausrichtung der Sensoren erreicht, die als Grundlage weiterer Analysen mit dem ALPIDE Teleskop dient.

Contents

1	Introduction	3
2	ALICE at the LHC	4
2.1	The Large Hadron Collider (LHC)	4
2.2	The ALICE detector system	5
2.2.1	The Inner Tracking System	6
2.2.2	The Time Projection Chamber	6
2.2.3	The Transition Radiation Detector	6
2.2.4	Outer detection layers	7
2.2.5	Quark-gluon plasma	7
3	Cosmic radiation	9
3.1	Interaction of radiation with matter	9
3.1.1	Ionization	9
3.1.2	The Bethe-Bloch formula	10
3.1.3	Coulomb scattering	12
3.2	Primary cosmic radiation	12
3.3	Secondary cosmic radiation	13
4	Semiconductor detectors	15
4.1	Basic semiconductor properties	15
4.2	Doping	16
4.3	The pn semiconductor junction	17
4.4	Hybrid sensors and MAPS	17
5	The ALICE Pixel Detector (ALPIDE)	19
5.1	ALPIDE architecture	19
5.2	Threshold and noise	20
6	Experimental setup	23
7	Analysis	26
7.1	Muon rate	26
7.2	Clustering	27
7.3	Initial alignment	29
7.4	Tracking, residuals and χ^2 -distribution	31
7.5	Alignment and event selection	34
7.6	Further alignment improvements	39
8	Conclusion and outlook	44
8.1	Summary	44
8.2	Comparison of measured muon rates with theoretical estimations	44
8.3	Cluster size and shape analysis	45
8.4	Tracking and alignment results	45
8.5	Outlook	46

Appendices	47
A.1 Acronyms	47
A.2 References	47
A.3 List of Figures	51
A.4 List of Tables	51
A.5 Additional Figures	52
A.6 Neutrino Interaction	53

Acknowledgement

Declaration

1 Introduction

The world of physics depends strongly on the research and development of new detector technologies to test the Standard Model of particle physics with unprecedented precision, and search for physics beyond. In the past 40 years developments on semiconductors have turned silicon tracking detectors into the number one tool to achieve high precision particle tracking in many high-energy particle physics experiments, such as the Large Ion Collider Experiment (ALICE) at the LHC in Geneva, Switzerland. Their compact design has made tracking close to the primary interaction point easier with each new upgrade and more and more achievements are being made each year, pushing for even higher precision and faster readout rates.

The confidence in what can be achieved with silicon has led to the proposal of a nearly pure silicon detector for the ALICE experiment at the LHC, including a nearly massless barrel detector consisting of ultra-thin silicon sensors with Monolithic Active Pixel Sensor (MAPS) technology, featuring an unprecedented low material budget, with the innermost layers possibly positioned inside of the beampipe of the LHC [1].

As these plans for the far future of ALICE are being made, there is an upgrade taking place right now. In the currently ongoing LS2 of the LHC, the ALICE ITS has been exchanged with silicon based MAPS sensors, called ALPIDE, that feature a high spatial resolution, fast readout rates and a very low material budget. A telescope of seven ALPIDE sensors was used this past year at the Gesellschaft für Schwerionenforschung GmbH (GSI) research facility in Darmstadt, to record, track and study cosmic muons. For a period of about one month, the setup was continuously taking data, resulting in nearly 300 000 particle events. This data can be used to study the behaviour of the telescope under unconventional conditions.

This thesis covers the aspect of the mode of operation and method of particle tracking and detector alignment, and serves as a foundation for further analysis strategies, while the other theses [2] and [3] are concerned with theoretical calculations about the angular distribution of cosmic particles, and a deeper understanding of the energy deposit and charge creation in the sensors.

In the first chapter, the ALICE experiment and its studies of quark-gluon plasma (QGP), are briefly discussed, followed by an introduction to the interaction of radiation with matter. Next, the concept of particle detection with semiconductor detectors is discussed, before characterizing the ALPIDE sensor and the experimental setup. Finally, the particle tracking approach is discussed in detail and the alignment results are presented.

2 A Large Ion Collider Experiment (ALICE) at the LHC

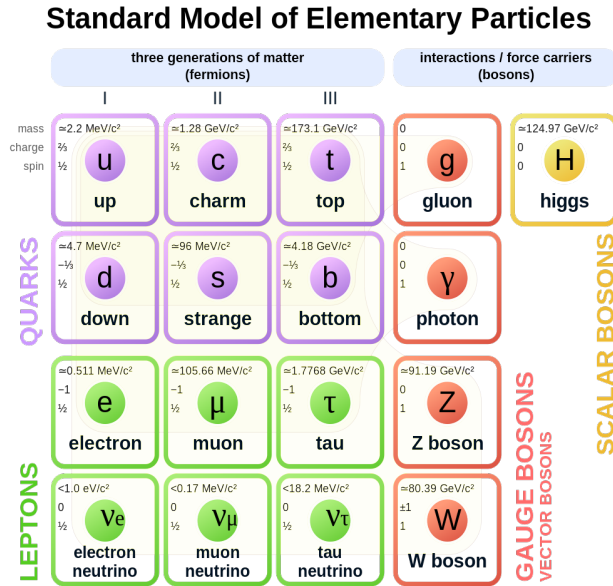


Figure 1: The Standard Model of particle physics [4]

In the Standard Model of particle physics there are 12 elementary particles (and their antiparticles), including six quarks, three charged leptons and three neutrinos, as well as five bosons (Figure 1). It describes three of the four fundamental forces¹: The *strong force*, the *weak force* and the *electromagnetic force*. The bosons are the mediators of these forces. The up- and down quarks are called the first generation of quarks. These make up hadrons, like protons and neutrons, and together with electrons they form atoms. The first generation particles make up most of the visible matter of the universe. Higher generation quarks and leptons are much rarer. They decay quickly into first generation particles and can generally only be observed in high-energy particle physics experiments, or cosmic radiation. As early as 1936 the muon has been discovered to be part of this cosmic radiation (subsection 3.2).

2.1 The Large Hadron Collider (LHC)

The LHC is currently the largest and most powerful particle accelerator. It primarily collides protons with energies up to 7 TeV [5], and reaches proton velocities that are just

¹The fourth force is the gravitational force, which is negligibly small on the tiny scale of particle interactions

about 3 m/s short of the speed of light. When particles collide at such high energies, they break apart into their elementary components, and occasionally, heavier particles are produced, like the strange-, charm- or bottom quarks which can then bind into new unstable matter².

The goal of a collider experiment such as ALICE is to reconstruct and understand this production of matter. This is achieved by the means of a variety of different detectors, that among other things, measure momentum, position and charge information for each and every particle. Only by reading out all this information it is possible to identify which particles are created and where they originate from.

At the LHC there are four main experiments dedicated to the research of high energy particle physics: ALICE, A Toroidal LHC Apparatus (ATLAS), Compact Muon Solenoid (CMS) and Large Hadron Collider beauty (LHCb).

2.2 The ALICE detector system

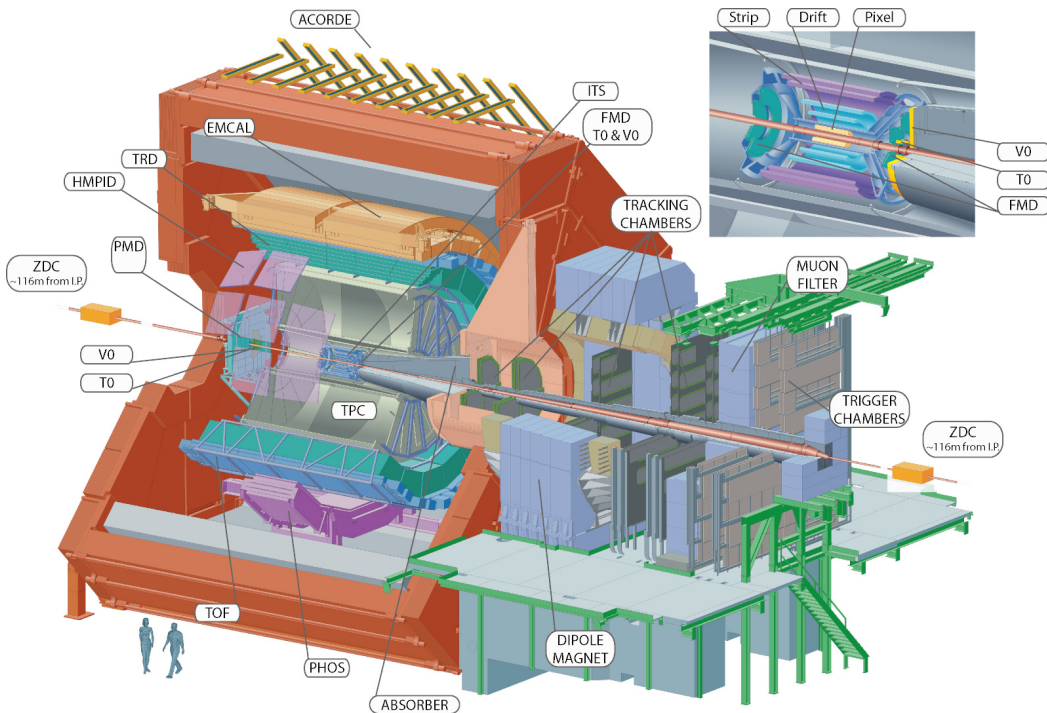


Figure 2: The ALICE detector system. For the acronyms consult the list of abbreviations (A.1) [6]

ALICE focuses on high-energy heavy-ion collisions. During a specific period of about one month per year, the LHC provides p-Pb and Pb-Pb collisions with a center-of-mass energy of up to 5.02 TeV per nucleon pair [7]. This opens the possibility to investigate a

²The top quark is an exception, as it has a very short lifetime, too short to bind into a hadron, and is therefore not detected

new state of matter, to which the ALICE collaboration has dedicated years of intensive research to: the Quark Gluon Plasma (QGP). To probe the QGP, one has to reconstruct the trajectory of as many particles coming out of the QGP as possible. For this, ALICE uses an advanced detector system, which is specially designed to meet the challenge of high particle multiplicities. A few detectors of special interest are detailed in the following section.

2.2.1 The Inner Tracking System (ITS)

The new ITS, which was implemented during the LHCs LS2, consists of seven concentric layers of the MAPS, discussed in this thesis³. The task of the ITS is to measure multiple points of the particle trajectory of an ionizing particle, while minimizing the deflection of the particle from its incident path. The ITS provides a spatial resolution of down to $4\ \mu\text{m}$ [8], and is designed to minimize the material budget, in order to reduce particle scattering (subsection 3.1). The sensors used are the ALPIDE sensors, which are very thin silicon pixel sensors encapsulating a matrix of 512×1024 (row \times column) $\approx 28 \times 28\ \mu\text{m}^2$ pixels (section 5).

2.2.2 The Time Projection Chamber (TPC)

The most important tracker of the central barrel is the Time Projection Chamber (TPC). It is capable of not only measuring many points along a particle track in three dimensions, but also provides information about the specific energy loss dE/dx of that particle. The TPC is a large, gas-filled cylinder, with a thin high-voltage electrode at the center. When a voltage is applied, an electric field along the beam axis is created. If an ionizing particle enters the gas volume of the TPC, it liberates electron-ion pairs. These electrons start drifting along the electric field lines towards the endcaps of the cylinder, where they are amplified by several layers of Gas Electron Multiplier (GEM) foils before inducing a signal in the pad planes. Two coordinates of the particle track are thus given by the signal on the endcap readout, while the last coordinate is given by the drift time of the ionization electrons. These spatial coordinates then allow for a full reconstruction of the particle trajectory. The particle's energy loss dE/dx is measured, if the amount of charge liberated is considered. Together, this information can then be used for Particle Identification (PID). As well as the ITS2, the TPC has been installed during the LS2 of the LHC, and has not yet been operated inside ALICE.

2.2.3 The Transition Radiation Detector (TRD)

The next layer from the central barrel is occupied by the Transition Radiation Detector (TRD). It uses the principle of transition radiation, which is radiation produced by charged particles when passing the boundaries of two materials with different indices of refraction, to identify electrons and positrons, and separate them from heavier hadrons. It is made up of six readout chambers in a stack, that each contain 3.2 cm thick polypropylene fibre mats. This step is crucial for PID, since it solves some of the ambiguity of the TPC. While the TPC handles the separation of different hadrons very well, it cannot reliably identify electrons. This is due to their lower energy loss, which causes them to overlap with other particles in the PID process (see Appendix 37).

³more on the functionality of semiconductor detectors in section 4

2.2.4 Outer detection layers

Further out are a number of detectors to finalize the PID-process. Four methods based on measurements of time of flight and ionization, transition radiation and Cherenkov radiation are used. Time of flight measurements are handled by the identically named Time of Flight (TOF) detector. It is a large-area detector based on multigap resistive plate chambers, with a time resolution of about 100 ps, and, among other things, is able to reliably separate pions from kaons [9]. While TOF identifies particles in the momentum range of around 1 – 4 GeV/c, high-momentum particles are measured in the High Momentum Particle Identification Detector (HMPID). It is a Ring Imaging Cherenkov Detector (RICH) used to identify particles with sufficient velocities to produce Cherenkov radiation⁴.

Next are two different calorimeters responsible for energy measurements of photons and electrons. They are designed for stopping electrons, positrons, as well as photons. The two calorimeters installed in ALICE are the Electro-Magnetic Calorimeter (EMCal) and the Photon Spectrometer (PHOS), that among other things help reconstructing high-energy jets.

The outermost layer is the ALICE Cosmic Ray Detector (ACORDE). It consists of plastic scintillator arrays and is used to measure cosmic muon events. It is also used to align the other detectors.

2.2.5 Quark-gluon plasma

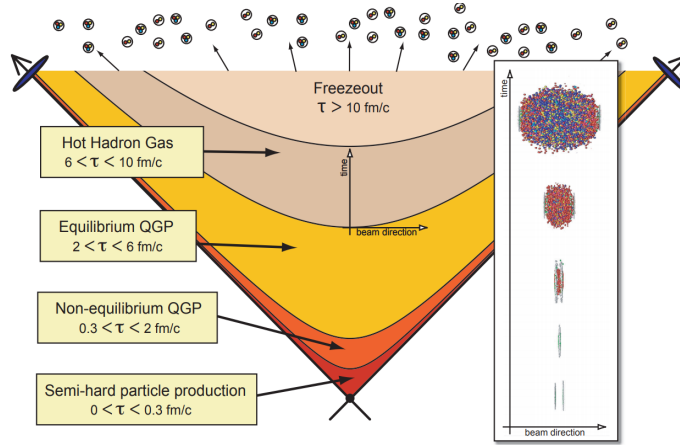


Figure 3: Schematic of the space-time evolution of the QGP created in heavy-ion collisions at LHC energies. The vertical axis represents time and the horizontal axis the space coordinate along the beampipe. Several stages of the QGP are denoted. τ denotes the time passed since the collision [11]

The QGP is an extreme state of matter that existed a few microseconds after the Big Bang [12]. The theory of Quantum Chromodynamics (QCD) explains, that at a certain

⁴The radiation a charged particle emits when passing through a medium with a velocity that is higher than the speed of light in that medium. A comprehensive explanation of Cherenkov radiation can be found in [10]

temperature ($T \sim 150$ MeV) or baryon density ($\mu_B \sim 0.5$ fm⁻³), a new phase of matter is formed, which manifests its physical properties in terms of nearly free dynamics of practically massless gluons and quarks [13]. This is because the coupling constant of the strong force α_s will grow asymptotically weaker for larger and larger momentum transfers or small distances between particles (asymptotic freedom of quarks). A simplified schematic of the formation of QGP in a heavy-ion collision is illustrated in Figure 3. When two heavy ions collide at ultra-relativistic energies, the area in which they overlap allows for hard collisions between partons (i.e. quarks and gluons). Their energy is sufficient to produce higher flavour quarks, which are essential for probing the QGP, as they experience its full evolution. The QGP lasts only about 6 fm/c ($2 \cdot 10^{-23}$ s) in which it constantly expands and cools down. Shortly after, the *chemical freeze-out* is reached, a phase transition in which hadrons begin to form. Their yield is now fixed, however, they are close enough together to still be subject to elastic scattering. After about 10 fm/c, they stop exchanging their momentum, referred to as *kinetic freeze-out*, as they make their way out towards the surrounding detectors. There, some of them will either be detected, or decay further and provide information about the properties of the QGP.

3 Cosmic radiation and interaction with matter

3.1 Interaction of radiation with matter

Particles traversing matter interact with it in some way. The weak interaction gets its name from its relative strength compared to the other forces. Because of the high mass of its exchange particles, the W^\pm and Z bosons, it is suppressed with respect to the other forces.

In the relevant energy regime⁵, the strong force is about 10^6 times stronger than the weak force. Only hadrons are affected by the strong force. Its exchange particle is the gluon, which only acts on the small scale of single nuclei (≈ 10 fm). Thus, for the purposes of this thesis, only the electromagnetic force is important. It is responsible for most important interaction processes, that allow particle tracking in modern high-energy physics experiments such as ALICE.

All modern detectors rely on the same principle for particle detection: the exchange of energy between some incident radiation and the detector material. Charged particles can deposit energy in a variety of ways, namely *ionization*, *excitation*, *bremstrahlung*, *Cherenkov radiation* and *transition radiation*, with ionization being predominantly used for particle tracking. The goal of a tracking detector such as the ALICE ITS is to measure many points of a particle trajectory while minimizing particle deflection. For charged particles, this is a challenge, because as soon as they enter the electric field of e.g. the nucleus of an atom, they will experience a force and change their direction. This can happen several times along the detector material and is therefore referred to as multiple Coulomb scattering (subsubsection 3.1.3). This effect is important to be considered (especially at low momenta), as it can result in non-linear tracks. This decreases the relative momentum resolution, which is why it is important to minimize scattering as much as possible. With the ALPIDE sensor, this is mainly achieved by using only a very thin layer of silicon (50 μm) to keep the number of interactions low.

3.1.1 Ionization

A lot of modern detectors rely on ionization for particle detection. In principle, ionization is the process in which a formerly neutral atom acquires a charge by means of losing one of its electrons. This effect is caused by an energy transfer between some kind of incident radiation and the electrons of the ionized atom. Because of their charge, the particles resulting from this reaction (one negatively charged electron and one positively charged ion) can be separated and accelerated by an electric field and collected by electrodes to create a signal. This is in principle how most gas detectors work. Without an electric field, the ionized particles remain free, and will usually quickly recombine under their own electrical attraction. Complementary for semiconductors, like ALPIDE, the principle of ionization is very important, as can be seen in the next section (section 4), though instead of electron-ion pairs, in a semiconductor electron-hole pairs are created.

A particularly interesting value to consider is the number of electron-ion pairs created by

⁵The energy achievable with modern particle accelerators. There is a point at which the coupling constant of the strong force reaches a value, which is smaller than that of the weak force. This energy is estimated by various sources (for example [14]) to lie somewhere around the order of magnitude of $10^{15} - 10^{17}$ GeV

an incident particle per unit length. One can consider an average number created for a given energy loss. Of course, this number is not equal to the energy loss divided by the ionization potential, since there are other processes to be considered. It turns out that for gases this average is in the order of 1 electron-ion pair per 30 eV, which means that for a particle that deposits 15 keV, an average of 500 electron-ion pairs are created. As a comparison, in a silicon semiconductor, the average energy required to create an electron-hole pair is only 3.6 eV.

Another important factor to consider is the motion of electrons and ions. In the absence of an electric field, most electron-ion pairs created will *diffuse* outward from their origin, against the gradient of concentration. The diffusing products will then quickly lose energy due to collisions with the atoms of the surrounding material, and eventually recombine. In the presence of an electric field, the electrons and ions are accelerated along the field lines until they reach a maximum velocity that is limited by collisions with the atoms in the material. This velocity is known as the *drift-velocity*. Naturally, it is much higher for electrons than for ions, because of their lower mass. For tracking primarily the signal of the produced electrons is measured, as it can be read out much faster. One can define the *mobility* of a charge as

$$\mu = u/E \quad (1)$$

where u is the drift velocity and E the electric field. It is usually measured experimentally. In semiconductors, electrons can generally reach velocities of around $3 \cdot 10^6$ cm/s [8], due to the strong electric fields across the depletion zone.

3.1.2 The Bethe-Bloch formula

In each interaction generally only a tiny fraction of the particle's total kinetic energy is lost. However, in relatively dense matter (i.e. most solids or liquids), the number of collisions per unit path length is so large, that this loss can be treated as a stochastic process. Although no prediction for each individual ionization process can be made, one can consider an average energy loss by ionization. This quantity is also referred to as *stopping power*, or simply dE/dx , and is calculated for heavy charged particles by the *Bethe-Bloch formula*:

$$-\left\langle \frac{dE}{dx} \right\rangle = 2\pi N_a r_e^2 m_e c^2 \rho \frac{Z}{A} \frac{z^2}{\beta^2} \left[\ln \left(\frac{2m_e c^2 \beta^2 W_{\max}}{I^2 (1 - \beta^2)} \right) - 2\beta^2 - \delta - 2\frac{C}{Z} \right] \quad (2)$$

with $2\pi N_a r_e^2 m_e c^2 = 0.1535$ MeVcm²/g

r_e : classical electron radius = $2.817 \cdot 10^{-13}$ cm	ρ : density of the absorbing material
m_e : electron mass = $9.109 \cdot 10^{-31}$ kg	z : charge of the incident particle in units of e
N_a : Avogadro's number = $6.022 \cdot 10^{23}$ 1/mol	$\beta := v/c$ of the incident particle
I : mean excitation potential	$\gamma := 1/\sqrt{1 - \beta^2}$
Z : atomic number of the absorbing material	δ : density correction
A : atomic weight of the absorbing material	C : shell correction

W_{\max} : maximum energy transfer in a single collision

A visual rendering of this equation for charged muons in copper can be found in Figure 4 (a). In particle physics, the area in which the energy loss of the particle is close to the minimum of the curve, is of special interest. This area is known as Minimum-Ionizing-Region. Because of their low energy loss, Minimum-Ionizing-Particles (MIPs) are used for

detector calibration and estimations for radiation shielding, and in many practical cases, relativistic particles like cosmic-ray muons are MIPs (see subsection 3.2).

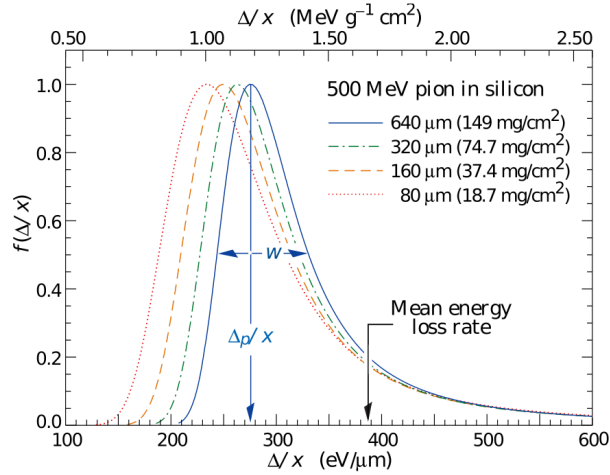
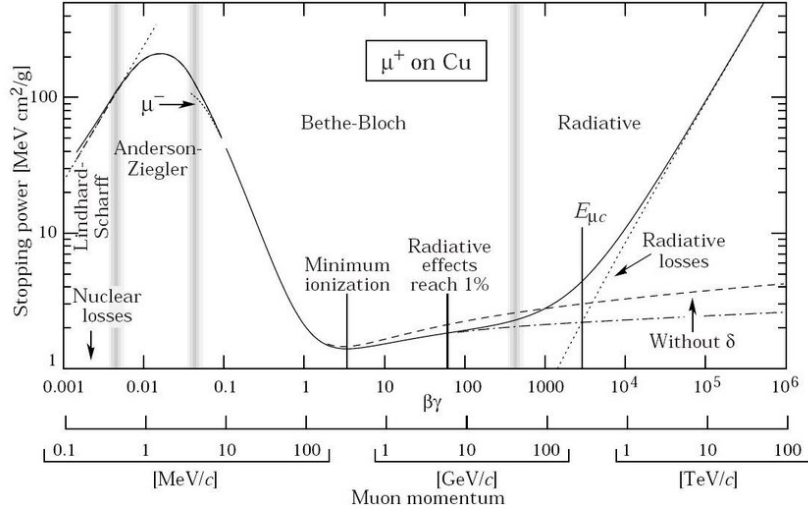


Figure 4: (a) Stopping power for muons in copper as a function of the particle momentum [15] (b) Straggling functions in silicon for 500 MeV pions [16]

For relatively thick absorbers, where the number of collisions is large, the energy loss distribution takes the form of a Gaussian. This is because the Central Limit Theorem (CLT) states, that the distribution of N random variables that are pulled from the same

statistical distribution will approach a Gaussian for the limit $N \rightarrow \infty$ ⁶. More complicated is the calculation of the energy loss in thin absorbers. If the number of collisions N is too small for the CLT to hold (e.g. in a very thin detector), one has to consider large energy transfers in a single collision. These events, add a significant tail to the high-energy side of the energy-loss distribution, giving it an asymmetric shape. This distribution was first calculated by Lev Landau⁷ [18], and can be seen for different detector thicknesses in Figure 4 (b).

3.1.3 Coulomb scattering

Electromagnetic interaction doesn't only result in a change of energy of a particle, but also its direction. At high energies, scattering angles are mostly small, but for relatively thick detectors, one can consider an average deflection angle after many gaussian distributed deflections. A statistical treatment of the process becomes possible (first described by Molière's theory [19]). In order to simplify scattering calculations, Highland [20] derived an elegant formula to calculate the mean deflection angle in a plane:

$$\theta_{\text{RMS}} = \frac{13.6 \text{ MeV}}{\beta pc} z \sqrt{\frac{x}{X_0}} \left(1 + 0.038 \ln \left(\frac{x}{X_0} \right) \right) \quad (3)$$

p : particle momentum

z : particle charge

x : thickness of material

X_0 : radiation length of material

The radiation length X_0 is a material-specific quantity that describes the mean distance over which an electron loses all but $1/e$ of its energy. It depends mostly on the atomic number A of the material. Because of its $1/\sqrt{X_0}$ -dependence, to minimize the scattering angle, light detectors should be used for particle tracking. Making them thinner (\sqrt{x} -dependence) further minimizes scattering.

3.2 Primary cosmic radiation

Cosmic radiation consists mainly of high-momentum protons and light atomic nuclei, which move freely through space, until they either hit an object, or come in contact with Earth's atmosphere. Typically, the energy range of those particles spans from 0.1 to a few GeV [21], although some can carry tremendous energies. The typical energy of these particles lies below the minimum-ionizing region of the Bethe-Bloch calculation [22], where the stopping power rises very quickly (Figure 4 a). This is why most of these particles usually don't reach far into earth's atmosphere.

⁶This is only true, if one assumes that the energy loss processes are independent from each other and the energy loss of the particle throughout the entire volume of the detector is negligibly small compared to the momentum, so that the velocity-dependent collision cross-section stays constant

⁷a more recent calculation has also been carried out by Hans Bichsel, using a convolution of a Landau and Gauß [17]. It yields more accurate results and will be used for correction in this thesis.

3.3 Secondary cosmic radiation and cosmic muons

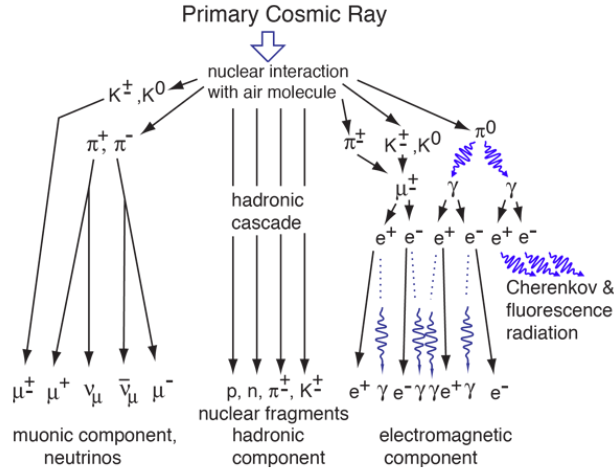
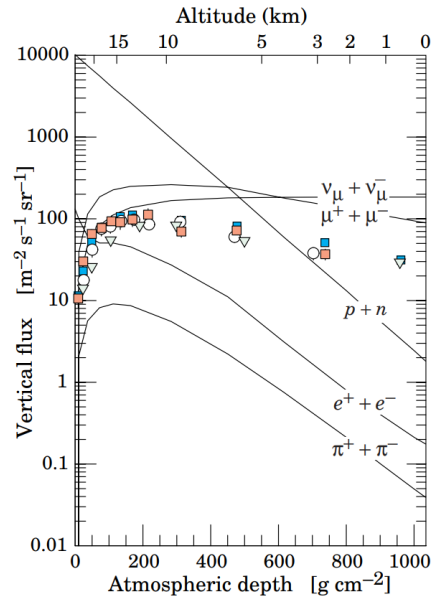


Figure 5: Secondary cosmic ray production in Earth's atmosphere [21]

Once a cosmic particle leaves the vacuum of space and approaches Earth, it quickly interacts with the atoms of the upper atmosphere. Nuclei are converted into secondary particles in what is called a hadronic shower. This way, a variety of particles of different type, mass, and charge are created (Figure 5). The charged pions and kaons created in this process then mainly convert into muon-neutrino pairs, and the neutral ones into electron-positron pairs and photons. Figure 6 shows the cosmic flux per altitude. Muons and neutrinos are (with a few exceptions) the only particles that are able to penetrate the entire atmosphere, and even some of Earth's surface⁸. This is due to the fact that muons have a relatively high lifetime compared to the lower lifetime mesons and a higher mass than the lower mass electrons, and only lose a small fraction of their energy while traversing matter. In fact, their minimum-ionizing region lies just inside of the typical energy range for cosmic rays, (see Figure 4 a) which makes them an excellent source for detector calibration. From Figure 6 a rate of about 100 muons per square meter per second ($100 \text{ m}^{-2}\text{s}^{-1}$) can be estimated. This number is going to become important later, as it serves as a first estimate of what to expect of the experimental setup.

⁸Neutrinos actually penetrate Earth entirely. In fact, it takes on average 250 000 Earths to result in a neutrino interaction. This is due to the incredibly low interaction cross sections of neutrinos. For a rough calculation of this number see Appendix A.6



(a)

Figure 6: Vertical fluxes of cosmic rays in the atmosphere with $E > 1$ GeV (estimated). The points show measurements of negative muons with $E_\mu > 1$ GeV [23]

4 Semiconductor detectors

Semiconductor detectors work on the principle of detection by ionization. However, instead of a gas, as explained so far, the medium is a solid semiconductor material. Instead of electron-ion pairs, electron-hole pairs are created, with the advantage, that only a very little energy deposit in the order of a few eV is needed to generate one electron-hole pair. This way the ionization yield (amount of charge created by the same energy deposit) is about an order of magnitude higher than it is for gas ionization. This does not only result in a higher energy resolution, but also creates the possibility of building very compact detectors.

4.1 Basic semiconductor properties

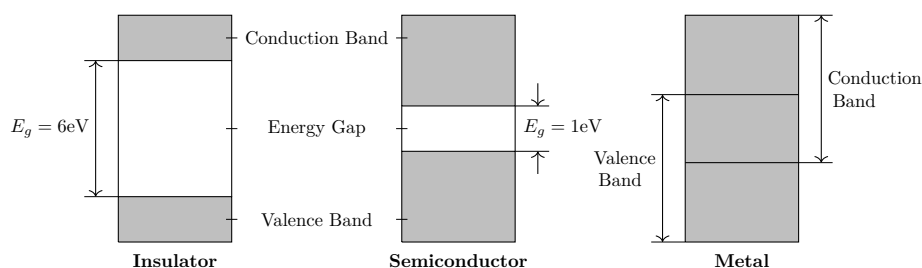


Figure 7: Energy band structure of different types of solids

Semiconductors are crystalline structures, that have special electrical conductivity properties. Because of Pauli's exclusion principle, there are only limited energy states in which electrons can fall into. Electrical conductivity arises, when electrons are *delocalized*, and can move freely through a material. On the other hand, insulation arises, when there are no free electrons. In an atom, energy levels that are close-by can be bunched into bands. The formation of bands is mostly a feature of the outermost electrons (*valence* electrons), which are involved in chemical bonding. The band these electrons reside in is called *valence band*. Higher energy electrons fall into the *conduction band*, and can move freely through the lattice. In between these two bands, there is a gap of forbidden energy states. To become delocalized, electrons have to be excited into the higher conduction band. In a metal, the energy gap is nonexistent, so that through thermal excitation, there are a lot of free electrons. In an insulator, the energy gap is very large, which means, that all electrons reside in the valence band. It is still possible for the electrons to reach the conduction band, e.g. when the material is heated up to very high temperatures, at which it becomes conductive again. Semiconductors are materials with an intermediately sized gap. For silicon, the gap is large enough for electrons to nearly completely reside in the valence band at room temperature. They can be excited by other processes, for example when a particle traverses the semiconductor, and ionizes the material. A schematic for the three types of solids is shown in Figure 7.

At 0 K all electrons in the valence band participate in covalent bonding between the lattice atoms. If the temperature rises, electrons can be excited into the conduction band, leaving

a vacancy behind in the lattice. Because the negative charge of electrons is balanced by the positive charge of the atomic nuclei, the absence of an electron (referred to as *hole*) leaves a net positive charge at the hole's location. If an electric field is applied, it is naturally very easy for a neighbouring valence electron to fill that hole. Repeating this process, the hole appears to be moving, and because of its positive charge relative to the electron, can be treated as a positive charge carrier. This means there are two sources of electric current in semiconductors: **electrons and holes** (electron-hole-pairs).

Analogous to (1), the drift velocity of electrons and holes under the influence of an electric field E , can be expressed as

$$u_e = \mu_e E \quad (4)$$

$$u_h = \mu_h E \quad (5)$$

where μ_e and μ_h are the mobilities of electrons and holes respectively. In silicon they are in the order of $1400 \text{ cm}^2/\text{Vs}$ for electrons and $450 \text{ cm}^2/\text{Vs}$ for holes [24].

4.2 Doping

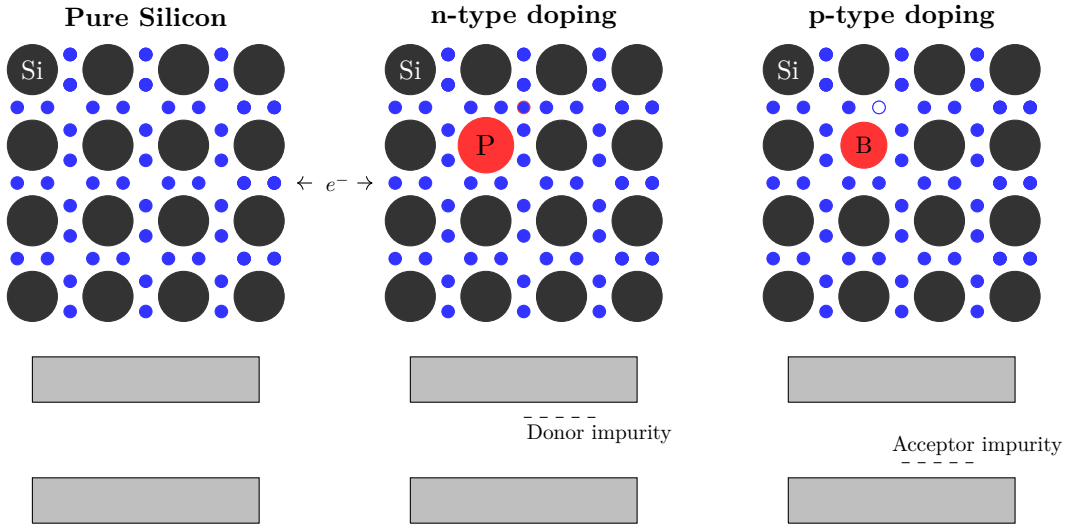


Figure 8: Silicon doping example with phosphorus (n-type) and boron (p-type)

Doping can be used to vary the conductivity of semiconductors by bringing in impurities into the crystal. Intrinsic silicon does not conduct currents very well, due to a limited number of free electrons. It has to be modified. The conductivity, or the inverse resistivity ρ of a semiconductor is given by

$$\sigma = \frac{1}{\rho} = e(n\mu_e + p\mu_h) \quad (6)$$

where e is the elementary charge, and n and p are the negative and positive charge carrier concentrations, respectively.

Silicon is tetravalent, so bringing in a pentavalent dopant (donor), adds an additional valence electron which does not fit into the valence band, thus additional energy states close to the conduction band are created. Electrons in these states can very easily be excited and increase the conductivity of the semiconductor. These materials are called *n-type* semiconductors. On the other hand, trivalent dopants (acceptors) bring in additional holes, which create energy states close to the valence band. These materials are called *p-type* semiconductors (Figure 8). Semiconductors with heavily concentrated impurities ($> 1\%$ concentration or higher) are indicated by a "+"-sign (n^+ -type / p^+ -type).

4.3 The pn semiconductor junction

To create a sensitive volume that can be used for particle detection, the formation of a *pn junction* is necessary. This describes the zone in between an n-type and a p-type semiconductor, that have been brought together, which has some special properties. Because of the different concentration of electrons and holes, an initial diffusion of holes towards the n-region and free electrons towards the p-region occurs near the pn junction. Because during this process, ionized and immobile atoms are left behind in the lattice, an equilibrium potential difference across the junction is created, which eventually halts the diffusion. Any electron or hole created in this junction will be accelerated and swept out by the electric field. This zone is called *depletion zone* and can be treated as an active volume for a detector. Without an external electric field, this depletion region generally only covers a fraction of the volume of the crystal. To increase its width, one can apply a *reverse bias* voltage. By attracting the electrons of the n-region away from the junction, and the holes towards the p-region, the depletion zone and sensitive volume of the detector enlarge ($d \sim \sqrt{V \cdot \rho}$ and the efficiency of charge collection increases (Figure 10). Therefore using high resistivity silicon is advantageous for particle detectors, because larger depletion regions (sometimes up to the entire crystal volume) can be achieved.

4.4 Hybrid sensors and MAPS

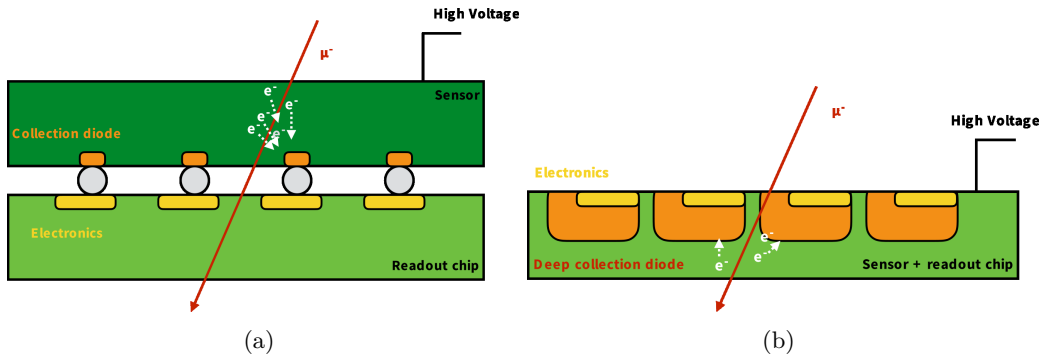


Figure 9: Schematic of a hybrid- (a) and a monolithic active (b) pixel sensor [25]

In many particle physics experiments, semiconductor detectors are part of a tracking system. The two most common types used are *hybrid pixel detectors* and *Monolithic Active Pixel Sensors* (MAPS). Hybrid pixel detectors consist of two separate layers - one for

electron-hole generation - as by-product of ionization from incoming particles - and collection, and one that contains the electronics needed for signal processing. The hybrid detectors have the advantage of two separate layers, that can be developed separately. The readout electronics can be reused for different sensors and are well separated from the high electric field in the sensor. They have been used in the ALICE ITS prior to the LS2 [26] of the LHC. This technology, however, has limitations in terms of material thickness and pixel size⁹, which inevitably have a negative effect on the spatial resolution of the detector.

A more modern, more complex method has been developed to include all the readout electronics directly on the pixel, and significantly reduce the sensor thickness. One example for this is TowerJazz's 180 nm CMOS Imaging Process¹⁰ which was chosen for ALPIDE. Although since everything is fabricated onto the same wafer, there is a possible influence of the sensor on the electronic circuitry and vice versa. Nevertheless MAPS have some very important advantages, some of which are a higher spatial efficiency, and a reduction in material budget, and therefore a reduction in multiple scattering.

⁹The bump bonds limit the achievable minimal pixel pitch to about 25 μm

¹⁰www.jazzsemi.com

5 The ALICE Pixel Detector (ALPIDE)

The ALPIDE sensor is a silicon-based MAPS. Its design allows for all the circuitry used for signal processing and read-out to be fabricated onto the silicon wafer and within each pixel, without significantly penalizing the charge collection. An experimental setup was used for the results presented in this thesis, which consists of a stack of ALPIDE sensors, with the goal of detecting and tracking muons.

5.1 ALPIDE architecture

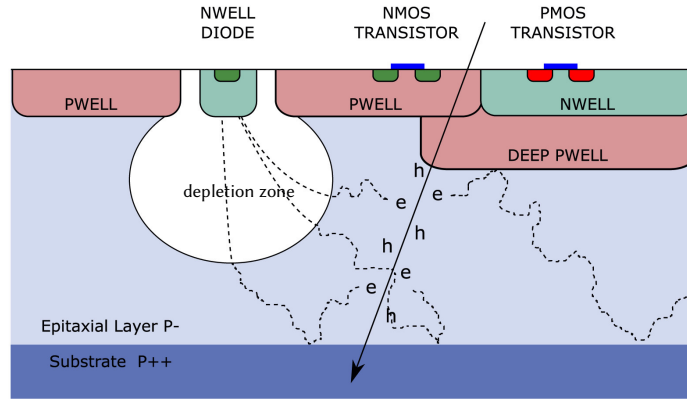


Figure 10: A cross section of a MAPS pixel, consisting of a p-type epitaxial layer and an N WELL-diode for depletion [27]

ALPIDE is a pixel detector, consisting of a matrix of 1024×512 pixels. The pixel dimensions are $29.24 \mu\text{m} \times 26.88 \mu\text{m}$ ($X \times Y$) [28]. With this, an estimate of the spatial resolution of the sensor in the case of no charge sharing can be made [29]. This is called *binary resolution* and in the case of ALPIDE turns out to be

$$\text{RMS}_{\text{binary}} = \frac{\text{pixel pitch in } x/y}{\sqrt{12}} \approx 8 \mu\text{m} \quad (7)$$

Note, that the binary resolution is only the resolution in case the particle is only detected by one pixel. If several pixels are involved in the particle detection, they form a so called *cluster*, which improves the position resolution of ALPIDE up to $4 \mu\text{m}$ [8].

Each pixel comprises a $25 \mu\text{m}$ thick epitaxial layer, which serves as the active volume of the detector, a heavily doped substrate P++ layer, and n-type and p-type implants on top of the epitaxial layer called *wells*. The only N-well, that is exposed to the epitaxial layer, acts as the collection diode for electrons, while p-wells accommodate the in-pixel circuitry (Figure 10). Based on the different types of semiconductors, there are two types of transistors, P-channel metal-oxide-semiconductor (PMOS)-transistors and N-channel metal-oxide-semiconductor (NMOS)-transistors, In order not to be limited to the use of NMOS transistors, (which can only be housed on p-type wells) ALPIDE features a deep p-well

to shield the epitaxial layer and prevent charge collection from a second n-well. The shielded n-well is then used to house PMOS-transistors. Signals collected by the collection diode are amplified via the in-pixel circuitry and stored in a multi-event-buffer (Figure 15). The signal shape and amplitude can be modified via on-chip Digital-to-Analog Converters (DACs)¹¹.

5.2 Threshold and noise

Certainly one of the most important parameters of most detectors is their *threshold*. The threshold determines the minimum amplitude of a signal that is required to identify a particle hit. Choosing a value that is too low, can result in *fake hits*, because of random thermal and telegraph noise¹². On the other hand, setting a threshold that is too high will result in the possibility of missing particles simply because the signal produced (i.e. the amount of electron-hole pairs created by a traversing particle) is too low to overcome the threshold. This can harm detection efficiency, and is why a careful consideration of the detector threshold is indispensable for any experiment dealing with particle detection.

ALPIDE can set an in-pixel threshold for the full matrix, which is controlled via a selection of DAC values. One selection is common to all pixels, but might result in slightly varying thresholds, due to slight differences in the material. It is possible to test the charge threshold via analog pulsing. With this method, a test charge can be inserted into the pixel through a pulsing capacitance $C_{inj} = 230$ aF. One DAC value corresponds to a voltage change of 7 mV, which considering the injection capacitance corresponds to ten electrons.

During a threshold scan, multiple injections for the same charge are performed. This is repeated for a number of charges up until a chosen limit is reached. This way, the detection probability over the injected charge can be obtained. The resulting curve is ideally a step function, which is smeared due to gaussian electronic noise, (Figure 11). The threshold can then be determined by finding the charge, at which the pixel will fire in 50% of the cases.

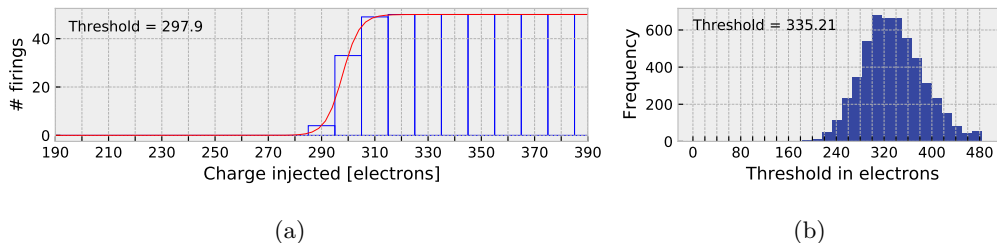


Figure 11: **(a)** Threshold scan of a single pixel. The pixel starts firing after an injection of around 290 electrons. The threshold is determined with an s-curve fit. **(b)** All thresholds from a single threshold scan of a sensor, performed on random pixels of that sensor

¹¹DACs are systems that convert a digital signal into an analog signal. They mostly come in the form of integrated circuits, and take the form of metal-oxide-semiconductor (MOS) chips.

¹²Random telegraph noise occurs in semiconductors and ultra-thin gate oxide films. It consists in sudden transitions between discrete voltage or current levels, and is suspected to be the main source of fake-hits [8]

The two main DACs used to modify the threshold are VCASN and ITHR. The threshold increases with increasing ITHR and decreases by augmenting VCASN. Figure 12 (a) illustrates the behaviour for a set of parameters at 3V back bias. Threshold scans are required to find the nominal operating point of a sensor, which lies around 100 electrons. There the signal-to-noise ratio is highest, while the detection efficiency (Figure 12 b) is still around 100%.

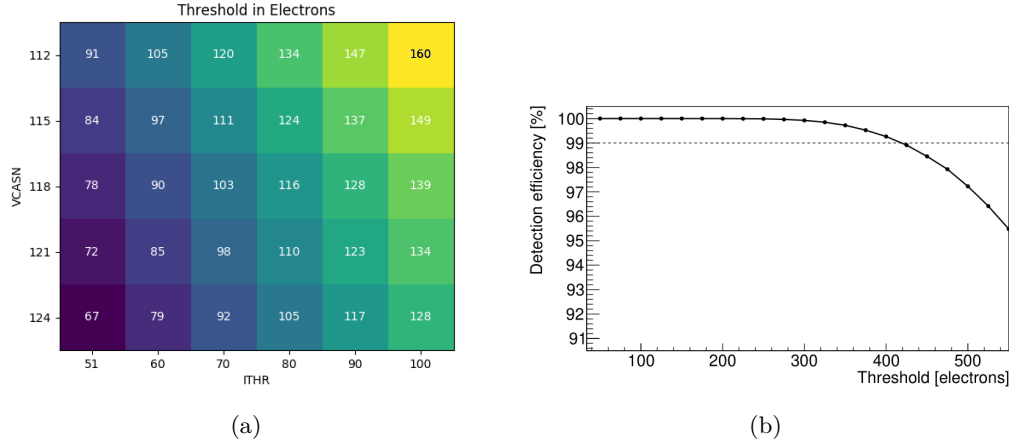


Figure 12: **(a)** Charge thresholds for different configurations of the chip parameters VCASN and ITHR. A value on the axis represents the DAC value of the parameter, which corresponds to voltages applied to the respective cascode transistor. The charge is measured in electrons and is calculated via the pulsing capacitance C_{inj} **(b)** (Simulated) sensor detection efficiency as a function of the charge threshold [8]

To investigate the fake hit rate of the chip, one can read out the multi-event-buffer a fixed number of times in the absence of any external stimulation. This way, every hit detected can be identified as a fake hit. Some of the hits will of course be actual particles originating e.g. from cosmic radiation, but this number is small compared to the large number of pixels tested simultaneously and can therefore be neglected. The fake hit rate can then be calculated by

$$\text{FHR} = \frac{\# \text{ of hits}}{\# \text{ of triggers} \cdot \# \text{ of pixels}}. \quad (8)$$

Figure 13 shows the fake hit rate for the ALPIDE sensor for two different configurations of the back-bias voltage V_{BB} (0V and $-3V$). It is clearly visible that the signal-to-noise ratio can be expected to be much better over the entire range when the collection diode is biased, than if no voltage was applied. The number of triggers limits the sensitivity of a measurement, it can therefore never be 0^{13} .

Applying a bias, one can clearly see an effect on the position resolution and efficiency on the sensor, as the depletion region grows. This however, will saturate at some point, and

¹³The sensitivity limit in a noise scan with 100000 triggers is in the order of 10^{-11}

the increase will only be minimal [30]. At $-3V_{BB}$ and thresholds in the nominal regime, the fake hit rate lies below 10^{-10} hits, meaning that for most pixels, less than one fake hit per ten billion hits can be expected. Additionally, this method allows identifying noisy pixels. These can be masked before measurements.

It is possible to plot the detection efficiency as a function of threshold, to determine the operational margins of the sensors (Figure 12 b).

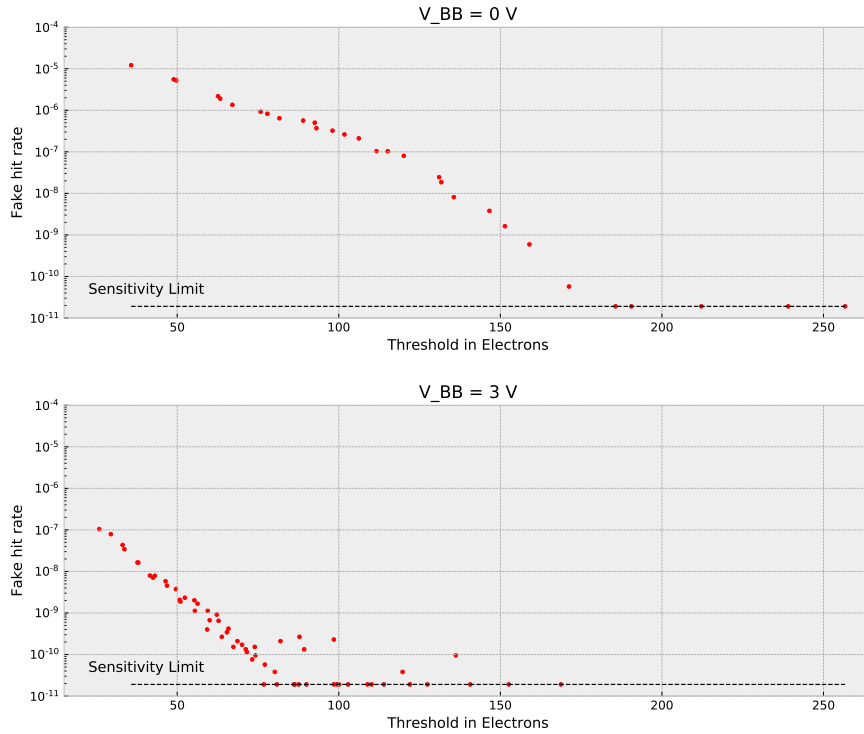


Figure 13: Noise occupancy without (top) and with (bottom) 3V back bias. Most of the noise on the chip disappears for thresholds over 100 electrons. It is assumed that during the measurement, cosmic radiation caused some pixels to fire, which explains the outliers above the sensitivity limit at higher thresholds. Another source for these hits can be random telegraph noise [8].

6 Experimental setup

The measurement was conducted in an experimental laboratory at the *GSI Helmholtzzentrum für Schwerionenforschung GmbH* in Darmstadt. The setup consists of seven ALPIDE sensors in a stack (*telescope*) with a 20 mm gap in between each plane (Figure 14).

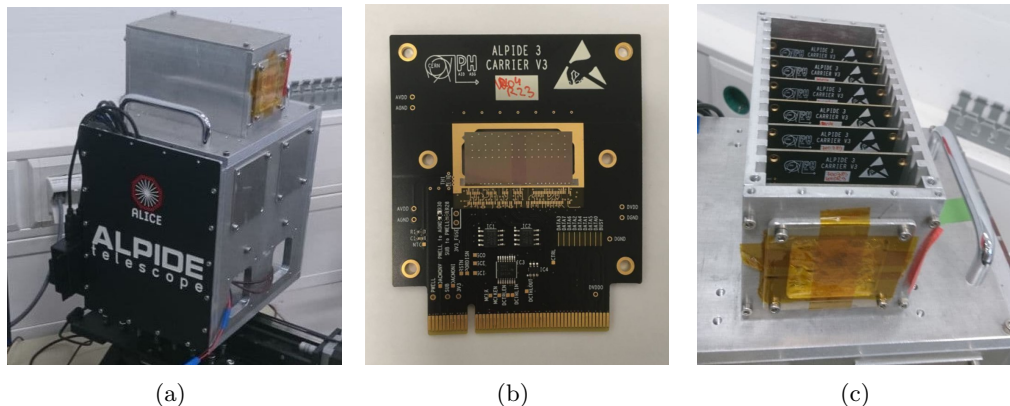


Figure 14: **(a)** The ALPIDE telescope **(b)** A single ALPIDE sensor on a carrier board **(c)** Sensors mounted inside of the case of the telescope

The telescope (Figure 14) holds all seven planes in place and shields the sensors from light. Below the sensors lies the casing that contains the Data Acquisition (DAQ) boards, which provide the readout and control functionalities, as well as power for the sensors. The DAQ boards are connected to a PC, and are programmed from there. A remotely operatable power supply is used for powering and biasing the chips.

The whole setup is rotated by 90° facing the sky, in order to detect cosmic muons, which have an energy of around 1 GeV. For this, a reverse bias voltage of 3V is chosen, which was proven to deplete a large part of the sensitive volume [8], and significantly improves the signal-to-noise ratio and detection efficiency.

The telescope relies on an external trigger and a strobe to store events. A simplified layout of the in-pixel circuitry is shown in Figure 15. Optimally, this setup would require a scintillator to serve as a trigger. However during the time of this experiment there were no scintillators available at the lab. Additionally, the goal is to detect cosmic muons, which are not as abundant as particles from a beam or collision experiment. It is actually advantageous to run this setup without scintillators. This way, the angle of acceptance of the telescope is vastly enlarged, since particles from every direction are accepted. Tracking can already be done if a particle hits only three of the seven available planes.

For this, a Nuclear Instrumentation Module (NIM) pulser with a period of about $96 \mu\text{s}$ is chosen. When charge is collected, there is a fast potential drop at the input node of the amplifying circuit (Figure 16 a). The reset then slowly ($\mathcal{O}(100 \mu\text{s})$) restores the potential to its nominal value. This potential drop is shaped into a shorter signal with a peak time of up to $10 \mu\text{s}$ (Figure 16 c). Additionally to the discriminator output, a strobe signal is applied with the beginning of each trigger. The discriminator stays asserted while the

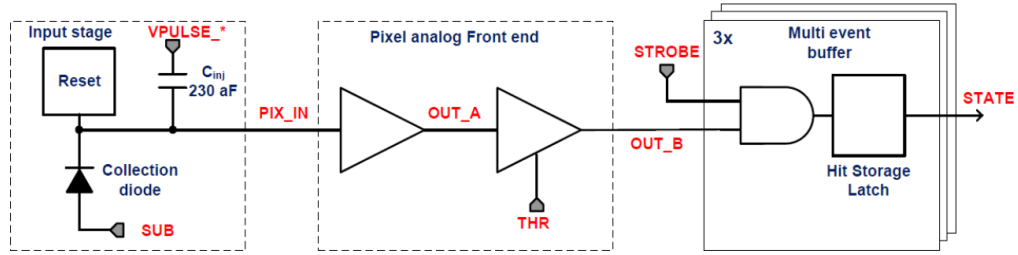


Figure 15: Schematic representation of the in-pixel circuitry implemented in the ALPIDE sensor [8]

signal is above the threshold. Only if the discriminator output is asserted at the same time as the strobe, its output state is stored into a register (Figure 16 c). Choosing a strobe length of $90 \mu\text{s}$, therefore yields a detector uptime of close to 100%, since the discriminator output always overlaps with at least one of the strobes.

For a consideration of the threshold the amount of electron-hole pairs created will be

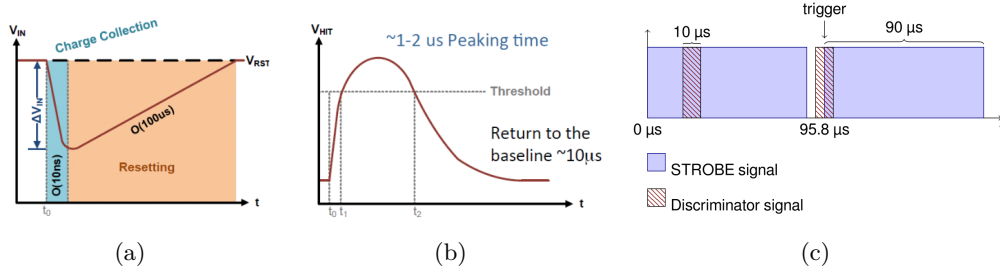


Figure 16: Graphical illustration of the in-pixel circuitry response to charge collection [30]. (a) Signal at the input node (b) Signal after shaping at discriminator input (c) Strobe and trigger signal

estimated for cosmic muons by using (2). The formula suggests that for muons close to the minimum-ionizing region, the energy loss in $25 \mu\text{m}$ silicon is 10.49 keV . This corresponds to roughly 2900 electron-hole pairs. However, Bichsel [17] suggests a factor of around 0.5 for the energy loss in $32 \mu\text{m}$ silicon, which should pose as a good reference for the $25 \mu\text{m}$ thick epitaxial layer. This means that the most probable energy loss of 5.25 keV would actually correspond to only 1450 electron hole pairs. Additionally, some of the charge might escape the pixel due to diffusion and be collected in a neighbouring pixel. With a few exceptions, this charge sharing can affect up to four pixels at a time, meaning that depending on the impinging location, the minimum amount of charge deposited in a pixel is about a quarter (360 electron-hole pairs) of the total charge. The threshold should lie well below this value. Looking also at the fake-hit rate, the sensor in the center of the telescope was chosen to be calibrated to a threshold of 127 electrons. The other planes were tuned to different, higher thresholds. This way, one can investigate the effect higher thresholds have on tracking, clustersize, and sensor efficiency, all with the same set of data. The low particle rate makes measurements of cosmic radiation very time consuming to perform,

and this method opens up several new paths to be taken during the analysis. Nevertheless, for most of these thresholds, an efficiency of close to 100% can be expected (Figure 12 b) and almost all of the muons should be detected.

Plane	Threshold [electrons]
0	272 ± 6
1	313 ± 6
2	228 ± 4
3	127 ± 5
4	214 ± 5
5	161 ± 6
6	202 ± 6

Table 1: Thresholds of all planes as configured in the experimental setup

To read out data from the detector, the data acquisition framework EUDAQ is used [31]. EUDAQ is designed to initialize, configure, stop and start the hardware, as well as read out the data and write it to a disk. The data of the telescope is stored in a `.raw` file format from which viable information has to be extracted. Usually, this is done by using the Corryvreckan test beam data reconstruction framework [32], designed for testbeam analysis. The large filesize however, makes it difficult to analyze the data in a normal way. With only a handful of particle events per file, the tracking algorithms designed for large datasets from testbeams fail. This opened the opportunity to do the tracking and alignment by hand, using tracks from angles, that are not usually available during a testbeam. Therefore, a simple translation from `.raw` to `.txt` was used, in which each event (consisting of all pixels hit during each strobe period) was written to a file in a readable format. Further analysis is then performed manually in Python [33]. In a single measurement, every event has its own ID assigned, which is just an integer number that is continuously incremented. To reduce filesize, and discard all the empty data, a loop over all files is performed, in which each non-empty event is assigned a unique global ID. All hits from each event are then stored into a Python object, and from there, the analysis chain starts.

Access to the lab was nearly impossible for most of the time during the measurement period, due to the COVID pandemic. Several issues during the measurement arose, and it was difficult to make any adjustments to the setup. Instead, steps were taken to control everything remotely, like a remotely operatable power supply.

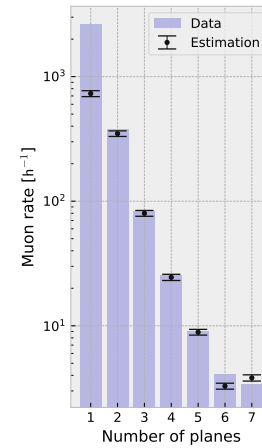
7 Analysis

7.1 Muon rate

To make estimations about the muon rate, one has to consider the angle of acceptance θ_n of the setup (i.e. the angle made by the normal vector of the planes of the telescope and traversing particle). One plane events (1p.e.) can be found with an angle anywhere from 90° to 31° . If the angle was any lower, a 2p.e. would be observed. This calculation is performed in detail in D. Schledewitz [2], who has been working on the same setup covered in this thesis. The resulting estimation for the muon rate is dependent on the number n of planes the particle traversed. The results can be found in Table 2. The calculated angles are based on a circular detector geometry with the same surface area of the sensor, and the center of the bottom most sensor defining the angle of acceptance.

n	θ_n	expected muon rate [h^{-1}]	measured muon rate [h^{-1}]
1	90	731 ± 40	2621
2	30.96	349 ± 18	379
3	16.7	80.0 ± 4.3	82.8
4	11.31	24.5 ± 1.4	25.4
5	8.53	8.89 ± 0.47	9.07
6	6.84	3.28 ± 0.18	4.05
7	5.71	3.82 ± 0.22	3.37

Table 2: Estimated muon rates, taken from [2], for different plane configurations. The multiplicities (i.e. the fact that for example a 6-plane event can consist of the upper six, or the lower six planes) has been considered.



The measurement was conducted in periods of eight to 17 minutes. 361 runs were performed in total, amounting to 93.6 hours of data taking. In total, 292582 events were recorded, only 3919 of which were detected by four or more planes.

The measured muon rates show a deviation from the estimation for one-plane events (1p.e.) and six-plane events (6p.e.). Other observations are contained within the uncertainty of the estimations. The reason for the huge amount of 1p.e. is a "hot" double column of pixels. On the uppermost plane, a bunch of pixels along a bus sometimes fired arbitrarily, amounting to a large number of supposed 1p.e. However, the goal is to do particle tracking, and since at least two planes are required to construct a track, the large number of 1p.e. won't have any effect on the rest of the analysis.

An explanation for the deviation of the rate for 6p.e. comes from the possibility that 7p.e. could be registered falsely due to one of the planes not detecting a hit. An estimation of the frequency of this error can be made by searching for all events where 6 planes were hit, with the seventh plane (which did not detect a hit in this case), being one of the inner planes. Since it is very unlikely, that two particles traverse the detector during the same time interval, this can essentially be treated as a 7p.e. with a gap in between (Figure 17). It turns out, that these events cover 8% of all 379 6p.e.

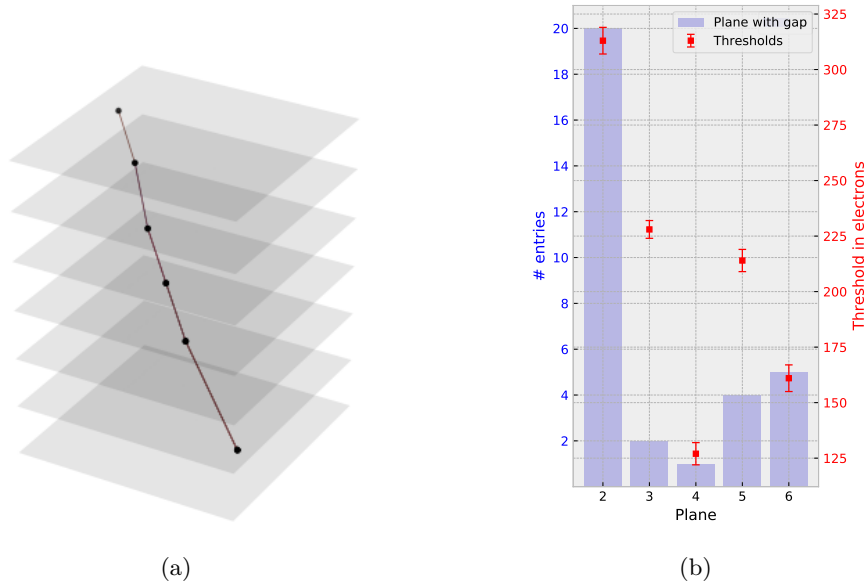


Figure 17: **(a)** 7p.e. disguised as a 6p.e. due to one of the planes not detecting a hit **(b)** Number of gaps counted per plane, and plane threshold. The gaps were found by searching for 7p.e., where one of the inner planes did not detect a hit. The high threshold of Plane 2 decreases the probability for that plane to detect a particle.

To find an explanation for the appearance of these gaps, one can look at the thresholds for planes 2-6 and plot them into a graph together with the probability for a gap to appear (Figure 17 b). The charge threshold for plane two is the highest across all planes. This is where also the most gaps were found when searching for these 7p.e. The ability of a sensor to detect a particle does not only depend on the threshold, but also on the amount of charge sharing, which varies on an event-by-event basis, which might explain the fact that the other planes do not exactly show the same phenomenon. Nevertheless, a clear trend is visible, and if higher statistics were to be used, the relation between charge threshold and detection efficiency is only expected to become more apparent. The fact that these gaps appear at all, also confirms the earlier calculated minimum energy deposit (section 6). It was estimated to be around 360 electron-hole pairs, which is very close to the charge threshold of plane two (313 electrons). In the end $\approx 6\%$ of all 7p.e. plane events were not detected by this plane.

7.2 Clustering

The next topic of interest is the identification of so-called *clusters*. A cluster is a group of fired pixels that lie close together. A particle that hits the detector creates charge by energy loss. This charge may spread through several pixels, forming a cluster. The particle trajectory can then be reconstructed with a higher resolution than the intrinsic resolution (7). Assuming that a particle, which crosses the pixel border, also activates the neighbouring pixel, different sensor responses can be identified. If the particle hits the pixel center, a single pixel fires. If it hits the border, two pixels fire, and if it hits the

corner, three or four pixels fire. Considering the areas for these responses, the pixel pitch is reduced, thus increasing the spatial resolution.

The aim of this thesis is to perform particle track reconstruction. To define a track, a minimum of two points in space are required. To increase the quality of the tracks, during the analysis, a minimum of four hit planes per particle event was chosen as basis for a track. A look at Table 2 reveals, that only 42 muons are detected by four or more planes per hour. It is therefore very unlikely for two muons to hit the telescope during the same trigger interval of 96 μs (section 6), and cause confusion between two hits. For now it can be assumed that all pixels, that fired during the same interval, come from the same muon¹⁴.

In order to track the particle, it is necessary to find the point on the plane, which best describes where the hit inside of a cluster might have occurred. For that, one needs to identify a group of fired pixels, that belongs to the same particle event. This is rather simple in the context of measuring cosmic muons. Due to the large time intervals between two events, it can always be assumed, that all hits from one event belong to the same particle. To find the impinging location of a particle, all pixel hit positions have to be averaged. In the case of ALPIDE, which is a binary sensor, there is no hit weighting, and the hit position is solely calculated by the arithmetic mean¹⁵. Figure 18 illustrates, how the cluster position and the position uncertainty is determined for different cluster sizes. The area of uncertainty is calculated from the standard deviation of the arithmetic mean.

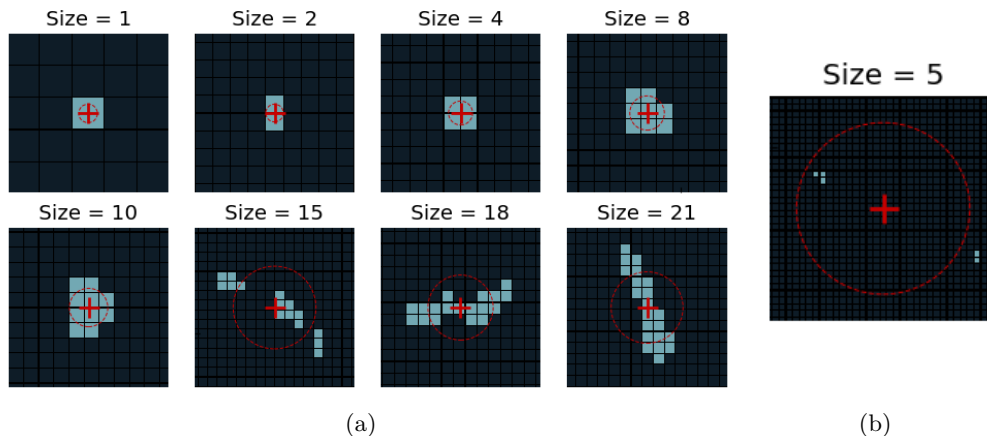


Figure 18: **(a)** Examples for clusters of different sizes, as they were detected during the measurement. The red cross indicates the average calculated position of all pixel hits (in blue) and the circle around it the uncertainty of the hit position. **(b)** Coincidental hit on a faraway pixel, that causes a false cluster center position and a large uncertainty.

The cluster size distribution (Figure 19) shows that the majority of clusters consist of only one or two pixels, and some fewer, larger clusters of three or four pixels. This has to do

¹⁴Except for a small amount of coincidental hits, resulting e.g. other surrounding radiation, which can be easily identified. More about this in subsection 7.5.

¹⁵Some sensors add a weighting to each pixel hit, for example, by measuring the time, in which the signal stays above the threshold [25]. This way a charge-weighted center-of-gravity approach can be used to obtain a more precise cluster center

with the tracking impinging point inside a pixel. If the particle hits the pixel in a small area around the center of the pixel, the lateral diffusion is insufficient to allow charge sharing and create a signal in the neighbouring pixels. If the hit occurs at the interface of two adjacent pixels, the volume might not be depleted and charge can spread and activate one or more neighbouring pixels. The number of two-pixel clusters nearly matches the number of one-pixel clusters. The same goes for three- and four-pixel clusters. If a pixel is hit in one of its corners, the charge may either spread to the two neighbouring pixels, or even three, which creates a square cluster. A detailed analysis concerning the pixel area and cluster probability is currently in preparation in [3].

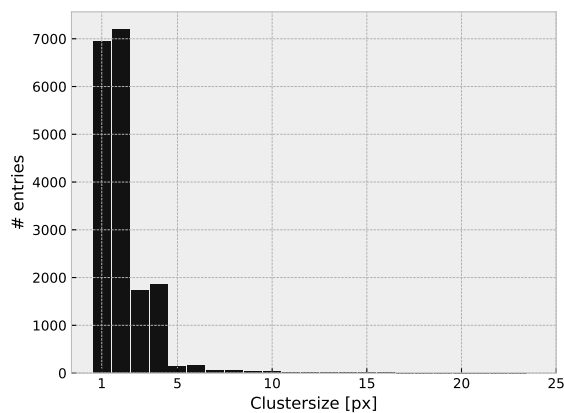


Figure 19: Cluster sizes for all events with four or more planes

Less likely cluster shapes, towards higher values of the clustersize appear when a particle hits the plane at a larger angle. This way, it may traverse multiple pixels, and deposit a lot more energy, increasing the cluster size. There are also some clusters that contain gaps. This is however a very rare phenomenon, which is still being investigated. Analysis on large angle particles are not easy to perform with this telescope setup. It is possible, for another setup, to rotate the planes, and intentionally track particles that hit the sensors in an angle, in order to further investigate the effect of charge sharing.

7.3 Initial alignment

In order to reconstruct and investigate the particle tracks properly, an alignment of the planes has to be applied to the data. Due to imperfections in the calibration and mounting, the planes have a slight offset relative to one another. The planes have to be shifted and/or rotated¹⁶ virtually, to increase the tracking quality. Usually, the first step to get a feeling for the alignment of a telescope is a spatial correlation plot between the planes. The correlation connects the impinging point of the particle on one plane (given by the

¹⁶Rotation is a second order effect. The ALPIDE sensors are encased in a rigid metal case with inserts for planes milled by a high precision CNC machine, to ensure precise spacing between planes, and leaving only little room for individual rotation. Test beam data indeed confirmed the rotation to be very small ($\approx 0.1^\circ$), so that rotation will be neglected for the scope of this thesis.

cluster position) with the impinging point on the next plane. If then each time the difference of the position coordinates is taken, for the case of a perfectly aligned detector, one expects a distribution that peaks around 0. Since a perfect alignment is impossible to do mechanically, instead the peak will be offset in one direction. This offset reflects the physical displacement of a detector plane in x and y with respect to all other planes. This translational misalignment is then corrected in a *prealignment* stage, by applying the correctional offset, to shift the distribution to zero, thus grossly correcting the mechanical shifts that are present.

As one would expect, the above is valid for straight tracks. For inclined tracks, as it is the case for cosmic muons, this method is less optimal, as the tracking data consists of mainly 4p.e. with a large angle, resulting in a wider spread distribution. Then, the low number of tracks poses an issue. Instead, alignment data from previous testbeams with the same detectors will be used for a coarse alignment of the setup.

In 2019 and 2020, the same telescope has been used at the Deutsches Elektronen-Synchrotron (DESY) testbeam facility to reconstruct electrons in order to characterize the sensor.

Testbeams are locations where beams of particles of well known energy are used to perform various tests to determine e.g. the efficiency, durability or resolution of a detector. The particles are usually directed orthogonally onto the sensor plane. Because of the large number of particles, a high-precision alignment of telescopes like the ALPIDE telescope becomes possible. The cosmic data has been recorded in between the two testbeam runs. Consequently, the true alignment of the planes used for data taking with cosmic muons lies somewhere in between the two testbeam alignments, as the displacement of the planes happened most likely during transportation back from- and to the facility.

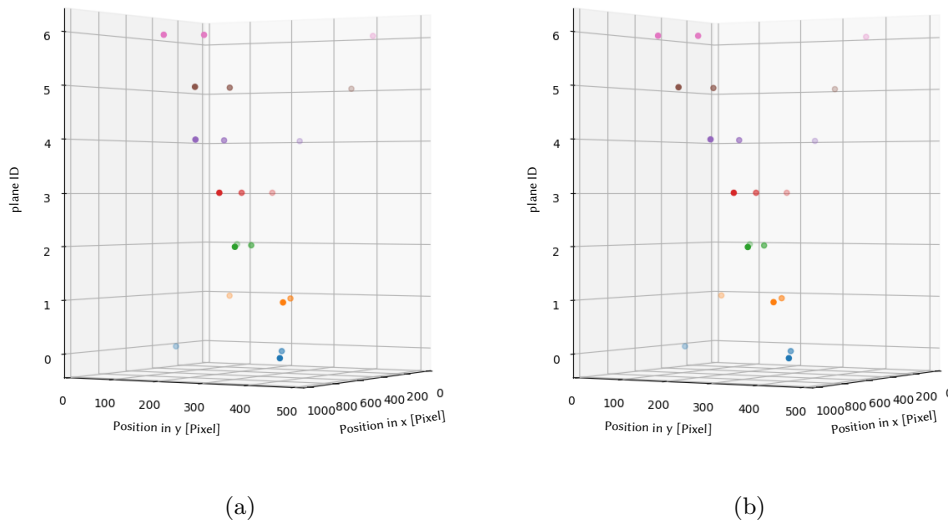


Figure 20: (a) Cosmic particle events with the alignment from the 2019 and (b) the alignment of 2020 testbeam data, before tracking. Plotted are three potential particle tracks, marked with points for each plane. The 2019 alignment yields slightly non-straight tracks, while the 2020 alignment seems to yield good straight tracks for different angles.

The data showed an offset of up to 1.8 mm of a specific plane between the testbeam campaigns. This shows, that during transportation back from the testbeam, the setup is slightly misaligned with respect to the testbeam data. Therefore a new alignment procedure needs to be conducted. To start off, after the first visualization attempts (Figure 20) it was found that the alignment data from the 2020 testbeam (presented in Table 3) was in best agreement with the alignment during the cosmics run. Therefore it serves as a decent starting point and further corrections are applied from here.

7.4 Tracking, residuals and χ^2 -distribution

Each cosmic muon event creates up to seven data points (hits) that can be used to construct a track in three-dimensional euclidean space. This track never perfectly intersects with the data points (unless only the minimum of two points is given), but rather approximates the path of the particle. This is because of the limited precision of the telescope. The tracking precision relates to the position resolution of the detector. Depending on several factors such as multiple scattering or misalignment, some tracks will lie closer to the actual hits than others, and some even seem to not fit the data points at all.

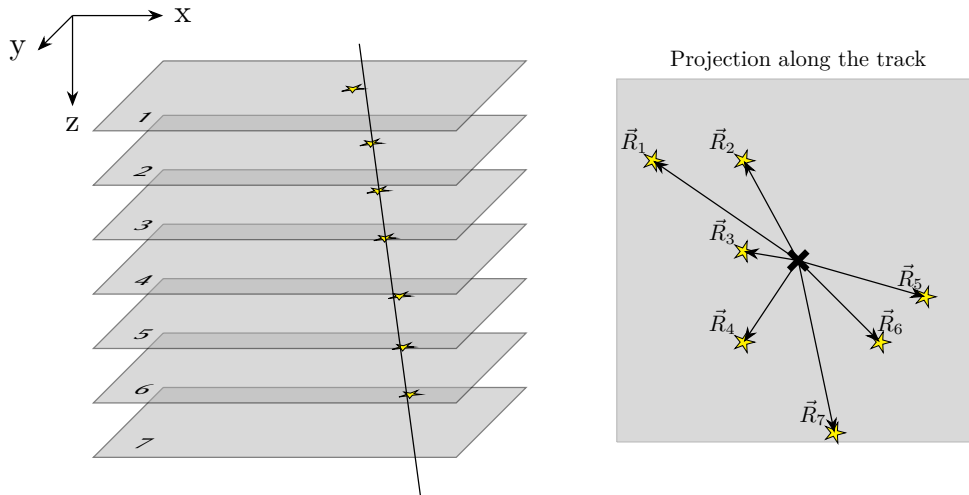


Figure 21: Schematic illustration of the calculation of residuals. The residuals result from position vector between the impinging location of the track (marked with a "x") and the particle hit location (marked with a "★").

It's important to characterize particle tracks based on their ability to faithfully represent the data. A procedure to control the quality of the tracks with respect to the actual hits is the *the goodness of fit*. The first step, is to calculate the *residuals* of the hits. A residual of a measurement is the difference between the measured value and the estimated value. In this case, the measured value is the cluster position on the plane, and the estimated value is the interpolated track intersect on the plane. An illustration of this calculation is shown in Figure 21.

Then, to obtain the goodness of fit of a track, a reduced χ^2 statistic analysis is applied

$$\chi_\nu^2 = \frac{\chi^2}{\nu} \quad , \quad \text{with} \quad \chi^2 = \sum_i \frac{|\vec{R}_i|^2}{\sigma_i^2} \quad \text{and} \quad \vec{R}_i = \vec{C}_i - \vec{T}_i. \quad (9)$$

χ^2 is the weighted sum of squared deviations \vec{R} (*residuals*). \vec{C}_i stands for the measured *cluster position* per plane, and \vec{T}_i the *track intercept* per plane i.e. the point where track and detector plane intersect. Figure 21 illustrates, how residuals are calculated. Both the cluster position and track intercept are not limited to the binary resolution of the telescope, but can be even more precise. $\nu = n - m$ is the number of *degrees of freedom*, and is composed out of the number of measured values n minus the number of fitted parameters m , and therefore depends on the number of planes that are included in the construction of the track. This is the reason why a *reduced* χ_ν^2 statistic analysis is applied. For example, if a 7p.e. is considered, there are seven data points with three coordinates each, so that $n = 21$ degrees of freedom. The number of fitted parameters, i.e. the minimum variables to define a straight line in three dimensions is 4 [34], so that $\nu = 21 - 4 = 17$.

Some examples for values of χ_ν^2 can be seen in Figure 22. A low χ_ν^2 -value means, that the track represents the data very accurately, and for the purpose of particle tracking, a value of $\chi_\nu^2 = 1$ is desired. A higher χ_ν^2 -value means, that the error is underestimated, and represents a bad track quality, while a lower value means that the errors are overestimated. Assuming that a particle track is constructed from seven hits, while each hit has a cluster size of 1 (a single pixel¹⁷), one can calculate back the mean distance from the track impinging points to the cluster positions on all planes:

$$d = \sqrt{\frac{\chi_\nu^2 \nu \sigma^2}{n}} \quad (10)$$

where $\sigma = 8.07 \mu\text{m}$ is the position uncertainty of a hit with cluster size 1 (which is equal to the binary resolution, defined in subsection 5.1), and n the number of hits that were involved in the creation of the track. Equation (10) is just a reverse calculation of equation (9) for the special case of clusters with size 1. Taking the first track from Figure 22 with a χ_ν^2 value of 7, the mean distance between track and each of the seven data points is only 31.43 μm . This means that per plane, the track is no further away than a pixel pitch from the cluster position. The mean distance for the other tracks are 320.95 μm and 606.36 μm for plot (b) and (c), respectively, which results in a significantly worse track quality.

¹⁷since we are dealing with minimum ionizing muons, this assumption is quite accurate, as most clusters aren't larger than one or two pixels (Figure 19)

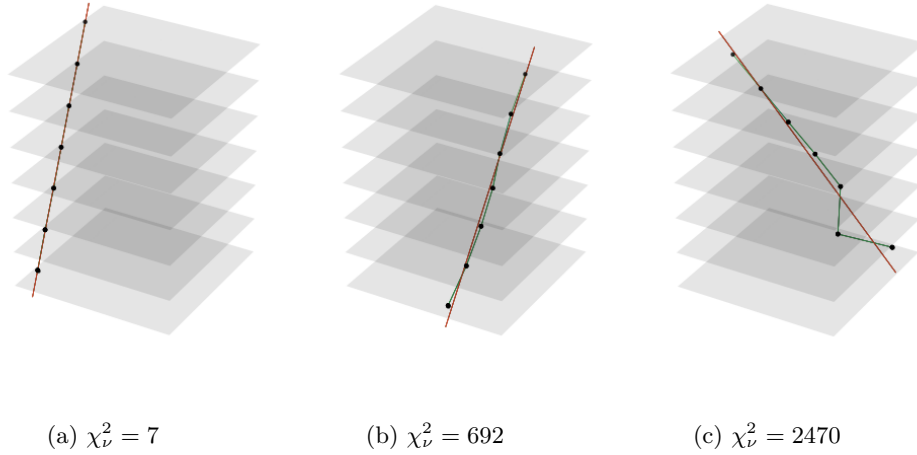


Figure 22: Cosmic muon track examples for different values of χ^2_ν . The black dots indicate the measured cluster position, and are connected by a green line (as an eye-guide). The red line is the interpolated track, an estimation for the particle path.

A look at the entire dataset reveals the alignment issue. Figure 23 (a) shows the different χ^2_ν -distributions for different numbers of planes involved in the particle event. For 7p.e. only, the statistics are very low, which is why for a complete analysis, all events down to 4p.e. will be included. This way, a peak is visible at around $\chi^2_\nu = 15$, irregardless for the number of planes involved. What is actually visible, are several different peaks at different locations, that are overlaying on top of each other.

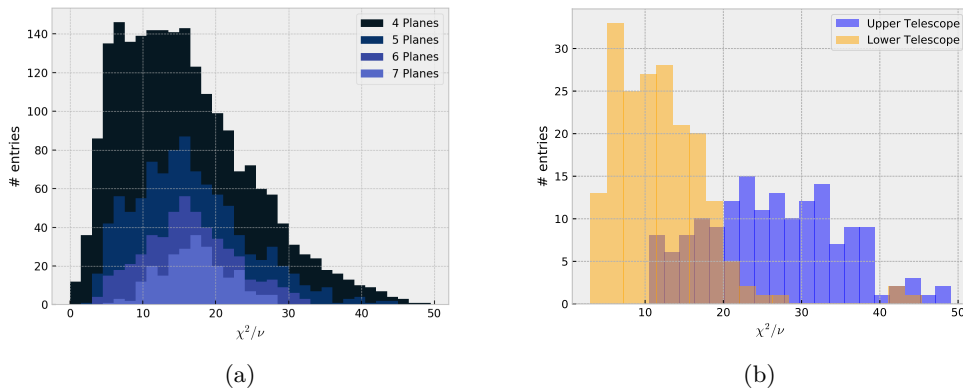


Figure 23: (a) χ^2_ν -distribution for all tracks that hit four or more of the seven planes. 4 planes in this context involves tracks that hit 4 or more planes. This includes all 5p.e., 6p.e. and 7p.e. (b) χ^2_ν for five-plane events, separated into particles that hit the top five, or bottom five planes

To clarify what is meant by that, Figure 23 (b) shows only 5p.e. but for two different configurations of planes. The orange distribution corresponds to events that only traversed through the lower part of the telescope, while the blue distribution corresponds to those that traversed the upper part. The meaning of this separation lies in the earlier mentioned plane misalignment. The upper two planes, seem to be much more misaligned than the bottom two. With this knowledge, an iterative alignment process can be conducted, by finding the translational offset of each plane, correcting it, and then repeating the tracking process, in an attempt to minimize the χ^2 -distribution.

7.5 Alignment and event selection

Before taking further steps though, another problem needs to be addressed, which is the random firing of pixels in some events.

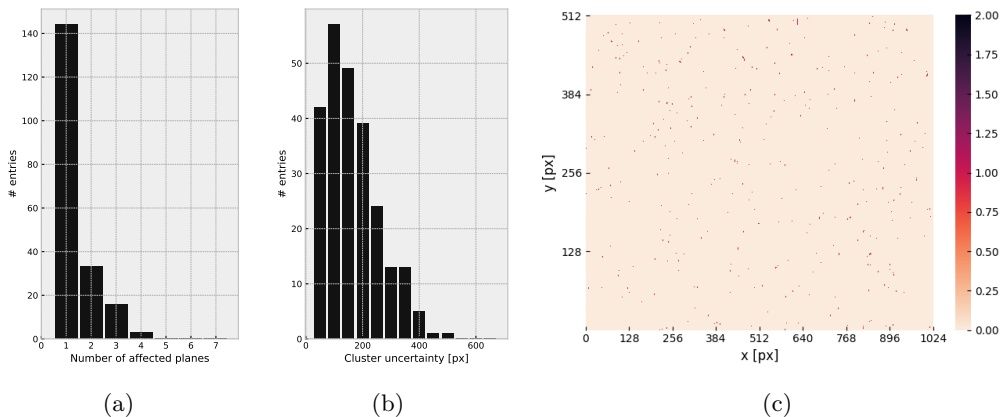


Figure 24: **(a)** Number of planes affected by a non-associated firing of pixels. **(b)** Cluster uncertainty distribution of associated clusters (as illustrated in Figure 18). **(c)** Hitmap of all hits related to a cluster with uncertainty above a certain threshold ($\sigma = 10$ pixels) - no specific region on the chips seems to be affected. Instead these occurrences happen uniformly across all planes.

About 6% of all 4 or more plane events contain contaminant clusters. A contaminant cluster is a bunch of pixels that fired during the recording of an event, and which usually lie far away from the actual particle hit. This position seems to be random, and most of the occurrences happen on one plane only (Figure 24). A correlation between this effect and the appearance of gaps in some of the 7p.e. earlier mentioned in subsection 7.1 could not be found, as some of the tracks which contained a gap were following a linear trend, while others seemed to deviate strongly from a straight line. It is believed for this effect to result from stray cosmics, hitting the telescope on one plane while another event is registered in the whole telescope. The probability that two particles traversed a plane in the same time interval is very low, but has to be accounted for. During tracking, a weighted position of all firing pixels on a plane is taken to construct the track. The tracks of these contaminated events therefore have very large deviations from the particle trajectories (see e.g. Figure 36 in the appendix). To exclude these events, a preliminary χ^2 -cut is performed at $\chi^2_p = 50$ (or a distance from track to the data points by approximately 3 pixel pitches). Discarding

any tracks with a higher χ^2_{ν} than this, should reduce the amount of tracks used to the ones that lie inside of the peak of Figure 23 (a), but increase the quality of the tracks, as only the straightest will be selected. Only a negligible amount include contaminant clusters, so that the remaining tracks can safely be used for alignment.

After tracking, the residuals of the remaining tracks (Figure 25) are calculated via a gauss fit, and then used to do a translational alignment. The residuals serve as a direct measure of the offset of each plane. Each residual distribution of the planes shows a slight offset from 0. A positive plane offset in one direction, results in a negative mean residual distribution. By subtracting the residual mean from the position of the planes, a much more accurate plane position is achieved. The error of the aligned position results from the standard deviation σ of the residuals.

Plane	Initial pos in x / y [μm]		Residual mean in x / y [μm]		Aligned pos in x / y [μm]	
1	0.0	/ 0.0	65.9 ± 22.1	/ 33.2 ± 17.7	-65.9	/ -33.2
2	318.4	/ -1261.5	-47.3 ± 37.6	/ -18.4 ± 27.1	365.8	/ -1243.0
3	177.2	/ 316.4	-20.2 ± 24.0	/ -53.8 ± 27.9	197.5	/ 370.2
4	-12.0	/ 186.0	-12.3 ± 26.4	/ 57.4 ± 23.0	0.2	/ 128.8
5	-757.0	/ 215.0	57.0 ± 23.9	/ -10.4 ± 22.1	-814.0	/ 225.5
6	-820.4	/ -917.1	-28.0 ± 20.1	/ -15.6 ± 18.1	-791.1	/ -902.3
7	-2336.6	/ -514.5	1.78 ± 17.9	/ 4.42 ± 18.6	-2339.4	/ -518.1

Table 3: Plane position with initial configuration from testbeam data, residual means, and plane position after alignment. In the testbeam alignment, plane 1 was used as a reference plane (displacement = 0), and all other planes were aligned with respect to that.

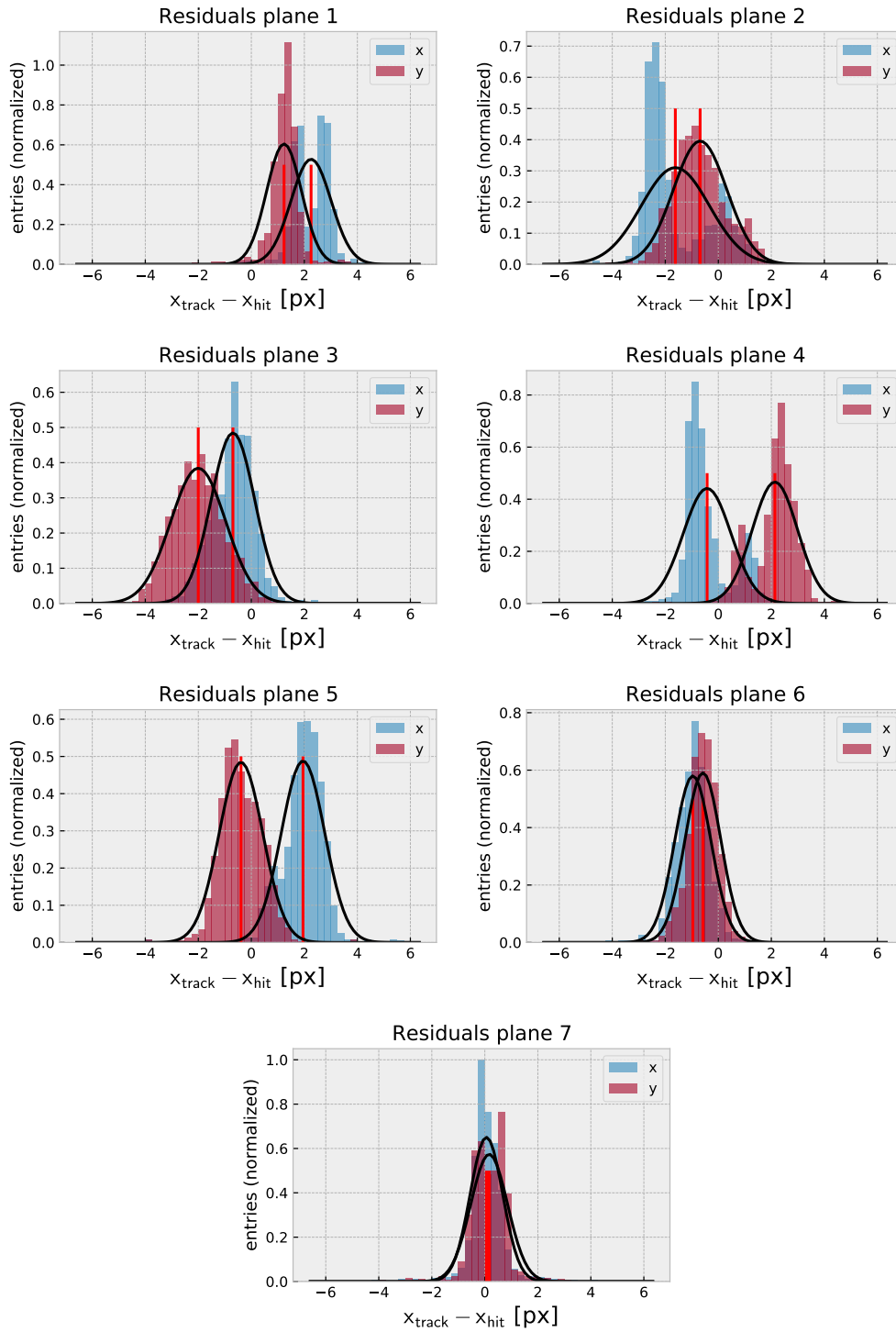


Figure 25: Residuals of all planes in x and y before alignment. A gaussian was fit to the data and the vertical lines (red) denote the position of the fitted mean.

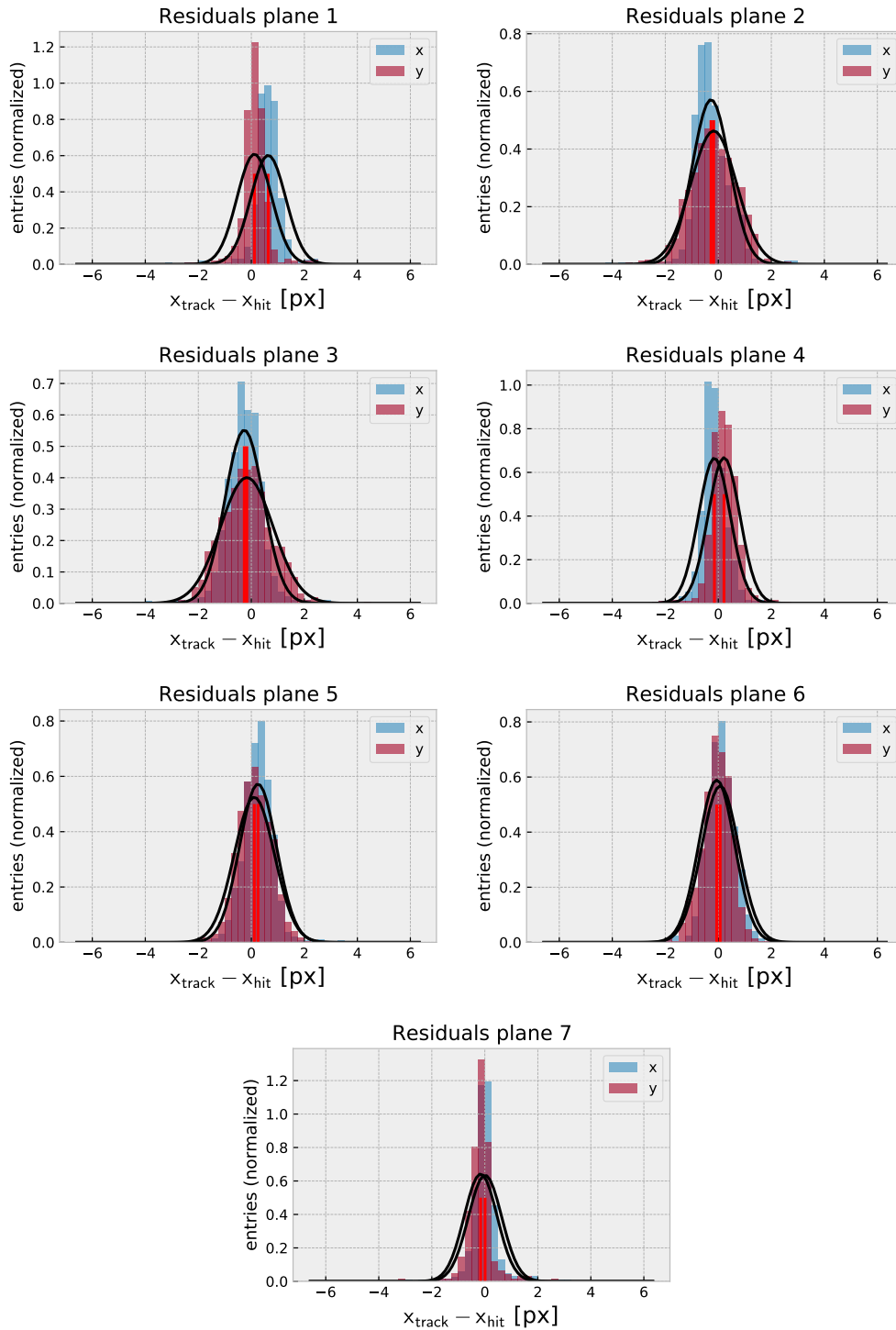


Figure 26: Residuals of all planes in x and y after alignment. A gaussian was fit to the data and the vertical lines (red) denote the position of the fitted mean.

Next, the entire tracking process is repeated. This significantly improves the χ^2_ν -distribution as can be seen in Figure 27 (a). A majority of the tracks now show a χ^2_ν -value close to 1. However, the width of the distribution can be further improved. By repeating the earlier mentioned steps, one can obtain an even more accurate alignment (Figure 27 b), however, returns are diminishing. Figure 28 shows, that after 3 iterations, only minimal differences in alignment are achieved, and a convergence can be identified. After 5 iterations, the alignment changes only by a hundredth of a pixel pitch ($\approx 200\text{nm}$).

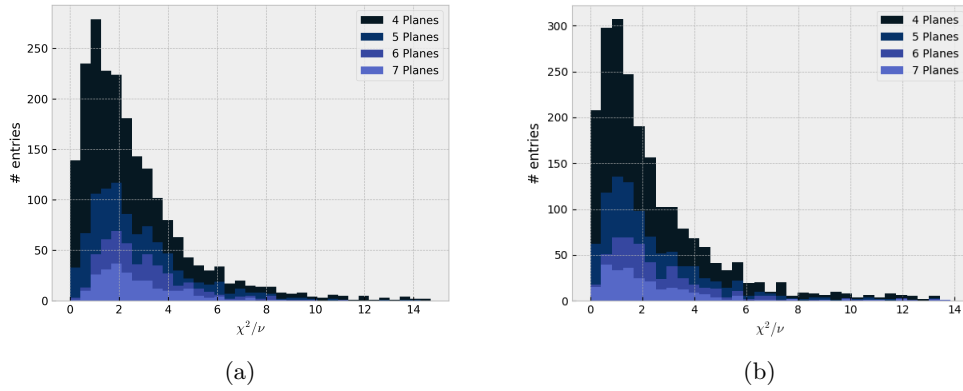


Figure 27: (a) χ^2_ν -distribution after one translational alignment and (b) after three iterations

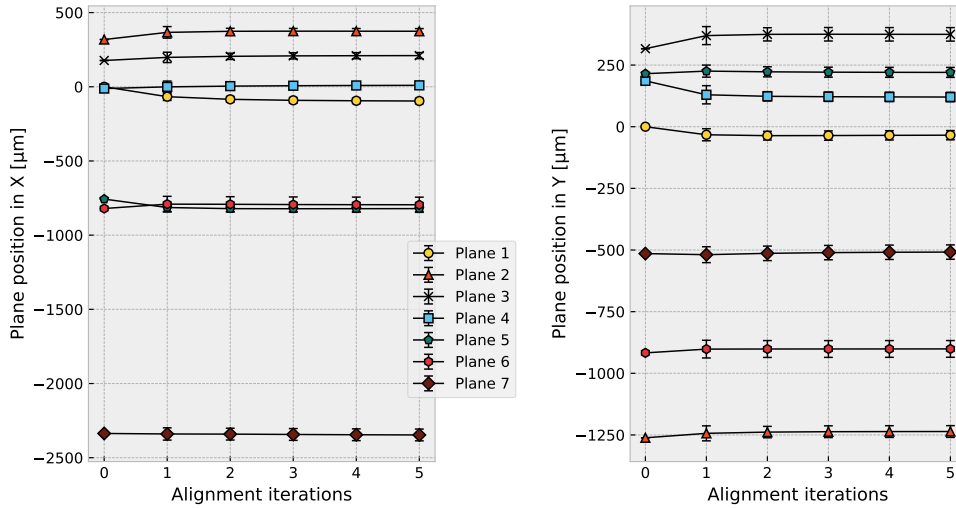


Figure 28: Plane position as a function of the alignment iterations performed. It can be observed that the alignment converges after only a few iterations, as there no visible change in plane position.

7.6 Further alignment improvements

The results of the alignment procedure show a clear improvement in track quality and a fast convergence towards a fixed value. However, it is not yet determined, if these values represent the actual displacement of the planes.

To test this method of alignment, a Monte Carlo model can be used to simulate a toy detector. This simulation has been performed and documented in detail by *V. Blobel*, at the *Institut für Experimentalphysik, Universität Hamburg* [35]. Blobel's paper shows that a purely residual-based iterative track fitting algorithm, as performed for the scope of this thesis, does in fact **not** converge towards the real detector displacement (Figure 30 a). The reason for this non-convergence is the fact that two degrees of freedom are yet undefined: a rotation of the telescope and a simultaneous shift (shearing) of all planes.

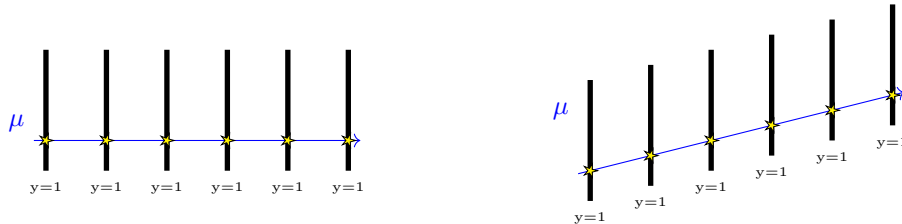


Figure 29: An example for a simultaneous shift of all planes (shearing of the telescope). Both alignments yield good track quality, but the right telescope has a strong bias and does not represent the actual alignment

In the case of cosmic muons, where the particle angle is large compared to the rotation of the telescope, rotation should not have a significant effect. It will be assumed, that the planes are parallel to the ground.

The second degree of freedom is illustrated in Figure 29. The previously used algorithm could converge to a sheared version (in either x- or y-direction) of the telescope. This would yield the same track quality, but different values for the displacement of the planes, and is therefore hard to identify. The amount of shearing depends strongly on the initial conditions that are given to the algorithm. To address this issue, one can fix the displacement of two planes, that are assumed to be carefully aligned externally, (setting it to 0) during the entire alignment process. Only the remaining planes are aligned. Although converging much slower, this approach actually converges towards the real misalignment in the simulated toy detector case (Figure 30). This approach is in fact used by several collaborations [36]. From now on, this method is going to be referred to as *fixed-plane* approach, while the former method is going to be referred to as *free* approach.

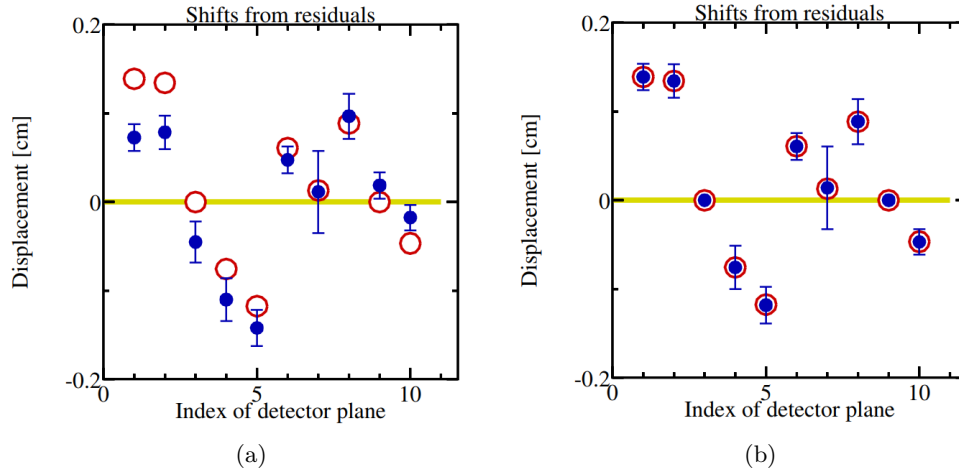


Figure 30: **(a)** Toy detector alignment with an iterative tracking approach including 10 planes. **(b)** Toy detector alignment using an approach, where two of the 10 planes are fixed, "not allowing" these planes to be aligned, but considering the displacement fixed at zero (for example, by assuming a careful external alignment). The red circles indicate the true alignment (displacement) of the planes, and the blue circles represent the displacement determined from the residual analysis. Both plots are the result of 30 alignment iterations. [35]

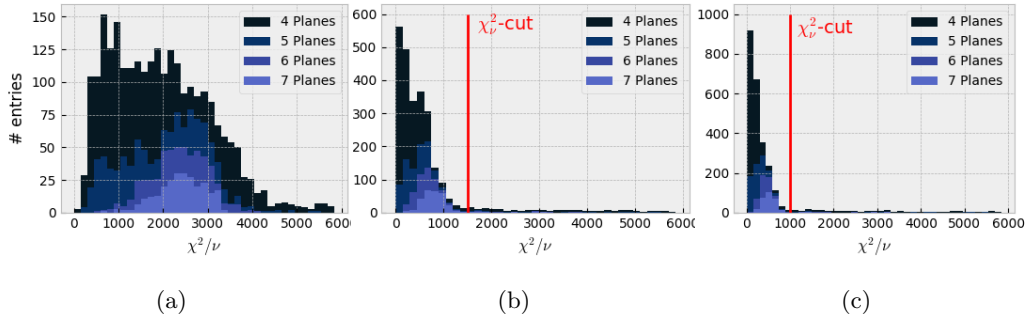


Figure 31: **(a)** χ^2_ν -distribution before alignment and after **(b)** one and **(c)** two iterations.

To apply this procedure to our data, plane 1 and 4 were chosen to be fixed, as their relative displacement is the lowest across all other planes (Table 3). This time, the alignment is not initialized with values from the testbeam, as it was in subsection 7.4. Instead, the position of all planes is first set to 0 in both x and y. This way, no preliminary event selection can be made, as all tracks have a really bad fit quality. The χ^2_ν values, vary from a few hundred to up to 4000 on average, which makes it difficult to identify contaminated events (discussed in subsection 7.5). Then, after the first alignment iteration, a χ^2_ν -cut at 1500 can be performed, and after the second iteration, a cut is performed at $\chi^2_\nu = 1000$, and so on. With each step, more and more bad tracks are discarded, while the majority of tracks is still preserved. The cuts have carefully been chosen in order not to discard too

many good tracks. An evolution of the χ^2 -distribution for the first few iterations can be seen in Figure 31. Figure 32 shows, that the alignment process is much slower, with plane 7 only visibly converging after over 60 iterations. The first change is rather large, with plane 7 being aligned over 440 μm in x-direction. In the second iteration, the difference is much smaller already with 164 μm . Again, the errors on all alignment steps result from the standard deviation of the residuals. As the planes are being moved closer and closer to their real position, the residuals decrease in width, and so does the error. In the end, 80 iterations are chosen to be performed for the final detector alignment. The final alignment is shown in Table 4.

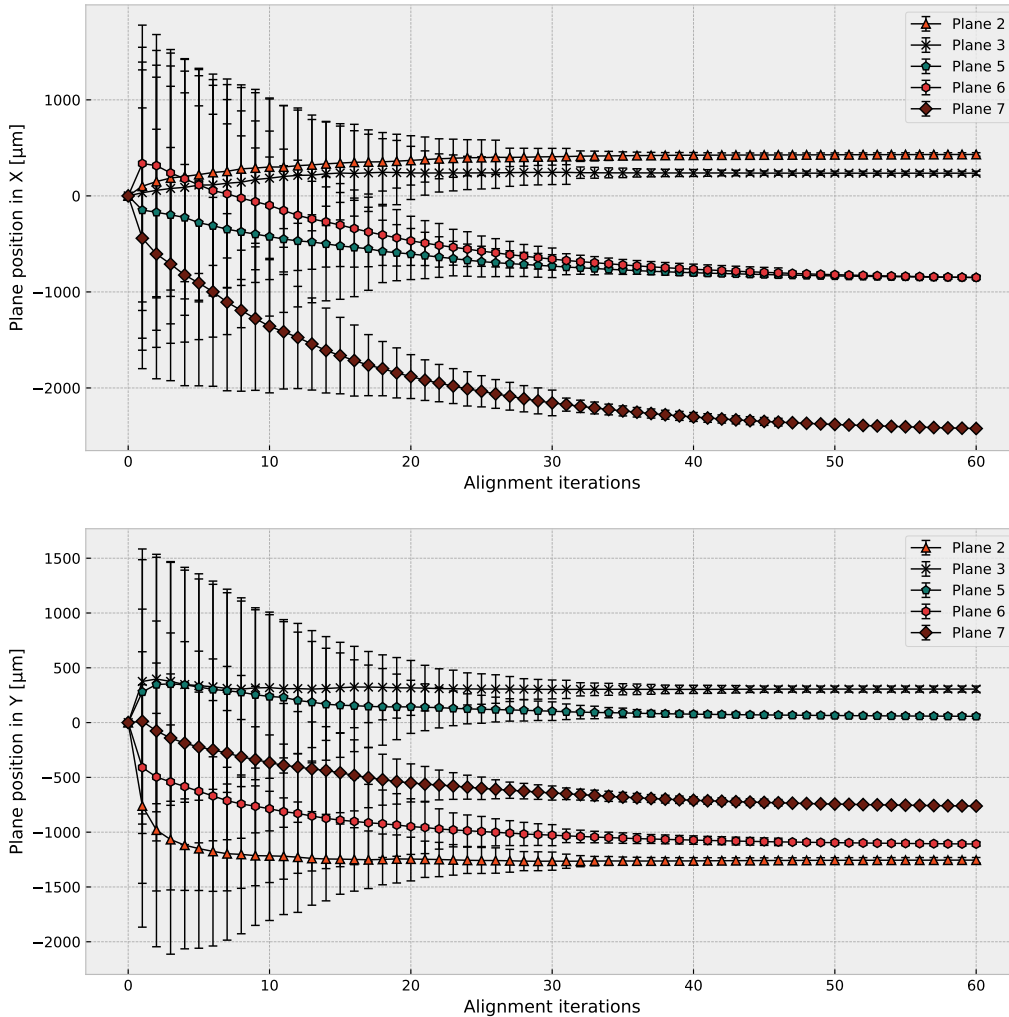


Figure 32: Plane position in x and y as a function of alignment iterations performed, using a fixed-plane approach. For improved visibility, only 60 of the 80 iterations performed in total are shown in this diagram

Plane	Plane position in x / y [μm]	
1	0.0 ± 0.0	0.0 ± 0.0
2	431.3 ± 18.4	-1255.1 ± 23.9
3	236.3 ± 20.8	305.68 ± 27.3
4	0.0 ± 0.0	0.0 ± 0.0
5	-849.9 ± 20.5	57.33 ± 20.2
6	-849.7 ± 20.3	-1107.9 ± 17.7
7	-2422.4 ± 18.7	-761.65 ± 16.1

Table 4: Plane position after alignment with fixed-plane approach

Next, both methods will be compared by their χ^2_ν -distribution. While it takes the fixed-plane approach about 80 iterations to converge, the free approach converges much quicker¹⁸. Both methods result in a very similar χ^2_ν -distribution, that peaks around 1, and therefore reach an overall very good track quality (Figure 33).

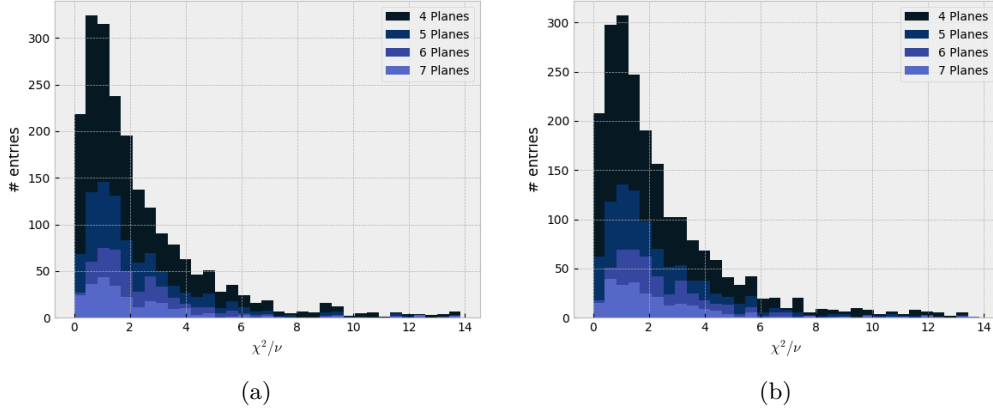


Figure 33: **(a)** χ^2_ν -distribution after 80 alignment iterations, using a fixed-plane approach, and for a direct comparison: **(b)** χ^2_ν -distribution after 3 iterations of the free approach

To directly compare the displacements of both methods to each other, the previous results of the free approach (Table 3) can be projected onto the alignment of the fixed-plane approach. This is done by simply shifting the alignment resulting from the free approach in a way, that both plane 1 and plane 4 will be positioned at 0. The shift of the other planes \vec{x} can then simply be described by a linear equation:

$$\vec{x}(z) = -\frac{\Delta\vec{x}}{\Delta z} \cdot z - \vec{x}_0 \quad z \in [1, \dots, 7] \quad (11)$$

where $\Delta\vec{x}$ is the positional difference in x and y between the two chosen planes and Δz the distance between the planes. \vec{x}_0 describes the displacement of one of the planes. This

¹⁸Even if no initialization is used, the algorithm converges in less than 10 iterations. A demonstration of this can be found in Appendix 38

projection slightly increases the error, but should result in a more accurate alignment. The result of this projection is presented in Figure 34.

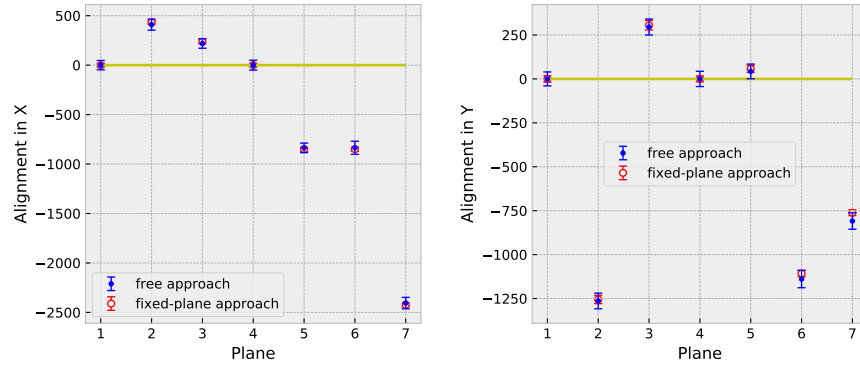


Figure 34: Comparison of the two alignment approaches used. The results of the free approach have been projected onto the results of the fixed-plane approach. The error of the projection is based on standard gaussian error propagation.

Both methods result in a very similar displacement. However, due to the elimination of one degree of freedom in the fixed-plane approach, the alignment can be assumed to be more accurate. If no projection is performed on the free approach, the displacement of both methods differ much stronger, and the effect of a simultaneous shift of all planes becomes much more apparent (Figure 35). The (virtual) shearing of the planes should always be accounted for. It depends heavily on the initial conditions of the alignment algorithm and can only be accounted for with some sort of reference, like another high-resolution detector, or a careful external alignment. For the analysis of cosmic particles it is important that the real angle of the particle is reflected in the detector alignment. The fixed-plane approach provides the best alignment achievable with this setup, without any external changes made to the planes.

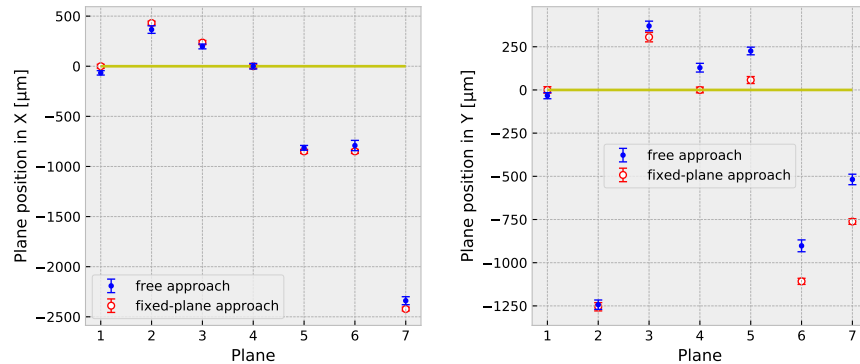


Figure 35: Comparison of the two alignment processes used, this time without projection. A clear deviation from the true alignment can be seen in the free approach.

8 Conclusion and outlook

8.1 Summary

Within the scope of this thesis, a telescope of seven ALPIDE sensors has been used as a cosmic muon detector at the GSI research facility in Darmstadt. For several days, the setup was measuring muons with an angle of up to 11.3° , given by the geometry of the setup. The measured data was compared with theoretical calculation of the muon rate. Data evaluation was performed from scratch including event categorization, clustering, and tracking. Two different alignment algorithms were developed, performed and compared, based on a statistical χ^2_ν -approach. 3000 particle tracks have been used to achieve an accurate detector alignment for the ALPIDE telescope. With this step, a foundation has been set, to further conduct studies for a better understanding of many of the effects mentioned in the analysis, and thus to increase their informative value, several proposals of supplementary experiments are given in the following.

8.2 Comparison of measured muon rates with theoretical estimations

In order to examine, if the measured events reflect the expected mean rate of incoming cosmic particles, the data was compared to theoretical calculations. It was found that for all measured events except those including only a single plane, the data fit well within the uncertainty of the experiment. A detailed analysis was performed by D. Schledewitz [2]. The very high rate of 1p.e. results from noisy pixels (pixels that registered a large amount of fake hits), specifically a single double-column of pixels along the same bus, that randomly fired during the measurement. The overall impact of these events on the analysis, however, is very small, since 1p.e. cannot be used for particle tracking, and are therefore excluded. They did, however reduce the total number of usable tracks, as many tracks were discarded in the χ^2_ν -cut.

The angle of acceptance of the setup is high, and therefore tracks with an angle of up to 11.3° can be reliably tracked. The actual maximum angle that can be detected with this setup is actually 29.2° , considering the rectangular shape of the detector. However, these events are rather unlikely, as the particles would have to cross the planes from one corner of the uppermost plane, to another corner of the plane, through which the particle exits. While it is advantageous to have a large angle of acceptance for cosmic muons in a setup like this (because the angle between the telescope and the ground is close to 90° and therefore only adds a negligible uncertainty), the operation without scintillators complicates the data evaluation drastically. Another approach would be to use scintillators to trigger the setup. Not only would this increase the track quality, it would make the setup able to run for longer periods of time, as less data is written to the disk (resulting in fewer crashes of the data acquisition software). The angular acceptance would be strongly decreased, so that instead for an analysis of muon angles, the entire telescope has to be rotated. Because this has to be done by hand, it would add an additional uncertainty to the measurement, but close to every possible particle angle could be measured. It is also to note, that a triggered setup would detect a much lower rate of particles, essentially making the experiment a lot more time-consuming.

Nevertheless, it has been proven [2], that the telescope can be used to measure the angular dependence of the rate of cosmic muons in good agreement with the estimation.

8.3 Cluster size and shape analysis

A particle can deposit charge which can laterally diffuse into other pixels. On each plane, the pixels that registered a hit form a cluster. The clustersize can reveal information about the angle, type and energy of the particle. A detailed cluster analysis of this experiment is currently in preparation by F. Franke [3]. Overall, the clustersizes agree with the expectation of cosmic muon clusters, ranging from 1-4 for most events. Only few events show strong deviations, and result usually from particles, coming in at large angles. Some clusters were found to contain gaps. This behaviour is currently not understood, but can be neglected for the scope of this thesis, as the occurrence of these clusters is very low. Figure 18 shows examples for most observed cluster shapes.

To do a more extensive study on cluster formation and charge diffusion, the statistics of this experiment would have to be vastly increased. Using only a low number of tracks, makes it difficult to reliably make statements about the formation of clusters, as less than 2000 clusters made of 3 or more pixels has been observed. Considering a plane has about half a million pixels, the number of clusters provided for an analysis should be around the same order of magnitude. This is where a scintillator would come in handy. Being able to measure consistently for long periods of time would simplify the acquisition of high quality tracks. Additionally, all planes could be rotated by a specific angle to increase the distance the particle traverses the epitaxial layer, essentially increasing the total energy deposit and number of electron-hole pairs, leading to the creation of larger cluster shapes.

8.4 Tracking and alignment results

For particle events, consisting of four or more planes, a tracking algorithm is implemented to analyze both particle angle, and the displacement of planes. It was found, that the planes of the telescope were shifted by up to 1.8 mm with respect to an earlier measurement performed at a testbeam. In an attempt to align the telescope with the cosmic data, two different iterative alignment approaches are performed, each based on a reduced χ^2 statistic. Initially, these χ^2_{ν} values are very large, as some of the planes show a strong misalignment, easily exceeding χ^2_{ν} values of a few hundred. A large number of tracks show extreme values of 10000 or higher, which is due to coincidental hits on one or more planes, registered during a cosmic particle event. These tracks however, are rejected, as they do not contribute to the detector alignment. The remaining tracks undergo an iterative alignment procedure, until an accurate alignment of the telescope is reached. The χ^2_{ν} distribution is minimized until it peaks as close to 1 as possible. Two different alignment algorithms are used, one of which aligns every plane individually during each iteration, which converges quickly until the telescope is reasonably well aligned. The second approach fixes two of the seven planes (i.e. setting their displacement to 0), before aligning the other planes. As outlined in subsection 7.6 the fixed-plane approach yields more accurate results, as a potential (virtual) shearing is prevented. The large track angles make a really efficient alignment possible with less than 3000 tracks available after the event selection.

8.5 Outlook

Now, that a good alignment of the setup is provided, there are several new interesting possibilities for the ALPIDE telescope. Apart from the above mentioned analysis strategies, there are several characteristics of the sensors that can further be investigated upon.

One of them is the sensor efficiency, which could be investigated by defining one of the planes as a *device under test* (DUT), and using the other six planes as a reference telescope. This way, the efficiency of the DUT can be measured as a function of charge threshold.

Applying the now well-known alignment to the reference telescope, the DUT could also be exchanged with other sensors. This way, the effect of neutron irradiation on the silicon could be studied with cosmic particles in order to identify damages to, or loss of efficiency of the sensor. This is usually done at testbeam facilities, with the testbeam commissioning carrying a large price tag. Cosmics however, are free, and constantly available.

Appendices

A.1 Acronyms

- ACORDE** ALICE Cosmic Ray Detector. 6
- ALICE** A Large Ion Collider Experiment. 3, 4, 6
- ALPIDE** ALICE Pixel Detector. 3, 6
- ATLAS** A Toroidal LHC Apparatus. 3
- CERN** European Organization for Nuclear Research. 3
- CMS** Compact Muon Solenoid. 3
- EMCAL** Electromagnetic Calorimeter. 3
- EMCal** Electro-Magnetic Calorimeter. 6
- HMPID** High Momentum Particle Identification Detector. 6
- ITS** Inner Tracking System. 3, 4, 7
- LHC** Large Hadron Collider. 3, 4, 7
- LHCb** Large Hadron Collider beauty. 3
- MAPS** Monolithic Active Pixel Sensor. 3
- MRPC** Multigap Resistive Plate Chamber. 6
- PHOS** Photon Spectrometer. 6
- PID** Particle Identification. 5, 6
- QGP** quark-gluon plasma. 4
- RICH** Ring Imaging Cherenkov Detector. 6
- TOF** Time of Flight. 6
- TPC** Time Projection Chamber. 5, 6
- TRD** Transition Radiation Detector. 6

References

- [1] D. Adamová et al. *A next-generation LHC heavy-ion experiment*. 2019. arXiv: 1902.01211 [physics.ins-det] (cited on page 3).
- [2] D. Schledewitz. “Measurement of the rate and angular distribution of cosmic muons with an ALPIDE telescope”. Germany: Physikalisches Institut Universität Heidelberg, Feb. 2021 (cited on pages 3, 26, 44, 45).
- [3] Felicitas Franke. “B.Sc. thesis - In preparation”. 2021 (cited on pages 3, 29, 45).
- [5] “High-Luminosity Large Hadron Collider (HL-LHC): Technical Design Report V. 0.1”. In: 4/2017 (Nov. 2017). Ed. by G. Apollinari et al. (cited on page 4).
- [6] Alessandro Ferretti. “The ALICE time machine”. In: *EPJ Web of Conferences* 58 (Sept. 2013), p. 02006 (cited on page 5).
- [8] Miljenko Suljic. “Study of Monolithic Active Pixel Sensors for the Upgrade of the ALICE Inner Tracking System”. PhD thesis. Feb. 2018 (cited on pages 6, 10, 19–24).
- [10] William R. Leo. “2.3 Cherenkov Radiation”. In: *Techniques for nuclear and particle physics experiments: a how-to approach*. Springer-Verlag, 1994, pp. 35–37 (cited on page 7).
- [11] Michael Strickland. “Anisotropic Hydrodynamics: Three lectures”. In: *Acta Phys. Polon. B* 45.12 (2014). Ed. by Michal Praszalowicz, pp. 2355–2394. arXiv: 1410.5786 [nucl-th] (cited on page 7).
- [12] Johann Rafelski. “Melting hadrons, boiling quarks”. In: (2015) (cited on page 7).
- [13] Sourav Sarkar, Helmut Satz, and Bikash Sinha, eds. *The physics of the quark-gluon plasma*. Vol. 785. 2010, p. 4 (cited on page 8).
- [15] Benjamin Cheymol. “Development of beam transverse profile and emittance monitors for the CERN LINAC4”. In: (Dec. 2011) (cited on page 11).
- [17] Hans Bichsel. “Straggling in thin silicon detectors”. In: *Rev. Mod. Phys.* 60 (3 July 1988), pp. 663–699 (cited on pages 12, 24).
- [18] L. Landau. “On the energy loss of fast particles by ionization”. In: *J. Phys. (USSR)* 8 (1944), pp. 201–205 (cited on page 12).
- [19] H. A. Bethe. “Molière’s Theory of Multiple Scattering”. In: *Phys. Rev.* 89 (6 Mar. 1953), pp. 1256–1266 (cited on page 12).
- [20] Virgil L. Highland. “Some Practical Remarks on Multiple Scattering”. In: *Nucl. Instrum. Meth.* 129 (1975), p. 497 (cited on page 12).
- [23] J.J. Beatty, J. Matthews, and S.P. Wakely. “Cosmic Rays”. In: *Astrophysics & Cosmology* 30 (2019) (cited on page 14).
- [27] M. Mager. “ALPIDE, the Monolithic Active Pixel Sensor for the ALICE ITS upgrade”. In: *Nuclear Instruments and Methods in Physics Research Section A: Accelerators, Spectrometers, Detectors and Associated Equipment* 824 (2016). Frontier Detectors for Frontier Physics: Proceedings of the 13th Pisa Meeting on Advanced Detectors, pp. 434–438 (cited on page 19).
- [28] ALICE ITS ALPIDE development team. “ALPIDE Operations Manual”. In: (July 2016) (cited on page 19).

- [29] Hermann Kolanoski and Norbert Wermes. “Anhang”. In: *Teilchendetektoren: Grundlagen und Anwendungen*. Berlin, Heidelberg: Springer Berlin Heidelberg, 2016, pp. 829–863 (cited on page 19).
- [30] Felix Reidt. “Studies for the ALICE Inner Tracking System Upgrade”. PhD thesis. Heidelberg U., Feb. 2016 (cited on pages 22, 24).
- [32] Jens Kröger, Simon Spannagel, and Morag Williams. *User Manual for the Corryvreckan Test Beam Data Reconstruction Framework, Version 1.0*. 2019. arXiv: 1912.00856 [physics.ins-det] (cited on page 25).
- [33] G. van Rossum. *Python tutorial*. Tech. rep. CS-R9526. Amsterdam: Centrum voor Wiskunde en Informatica (CWI), May 1995 (cited on page 25).
- [35] V. Blobel. “Software alignment for tracking detectors”. In: *Nucl. Instrum. Meth. A* 566 (2006). Ed. by R. Bernhard et al., pp. 5–13 (cited on pages 39, 40).

Webpages

- [4] Cush MissMJ. *Standard Model of Elementary Particles*. Sept. 2019. URL: https://upload.wikimedia.org/wikipedia/commons/0/00/Standard_Model_of_Elementary_Particles.svg (cited on page 4).
- [7] *Facts and Figures about LHC*. 2020. URL: <https://home.cern/resources/faqs/facts-and-figures-about-lhc> (cited on page 5).
- [9] Alexander Akindinov. *ALICE revolutionizes TOF systems*. 2011. URL: <https://cerncourier.com/a/alice-revolutionizes-tof-systems/> (visited on Oct. 25, 2011) (cited on page 7).
- [14] Richard Jacobsson James Gillies. *The coupling constants and unification of interactions*. 2001. URL: https://www.physicsmasterclasses.org/exercises/keyhole/en/projects/running_alphas.html (cited on page 9).
- [16] Johanna Stachel. *Detectors in Nuclear and Particle Physics*. Apr. 2015. URL: physi.uni-heidelberg.de/~sma/teaching/ParticleDetectors/stachel_2.pdf (cited on page 11).
- [21] Carl R. Nave. *Cosmic rays*. 2017. URL: <http://hyperphysics.phy-astr.gsu.edu/hbase/Astro/cosmic.html#c2> (cited on pages 12, 13).
- [22] Particle Data Group. *Detectors in Nuclear and Particle Physics*. 2019. URL: <https://pdg.lbl.gov/2020/reviews/rpp2020-rev-passage-particles-matter.pdf> (cited on page 12).
- [24] *NSM Archive - Physical Properties of Semiconductors*. 2020. URL: <http://www.matprop.ru/> (cited on page 16).
- [25] Jens Kröger. *Characterisation of Silicon Pixel Sensors for High-Energy Physics and beyond*. Version 1.0.2. July 2020. URL: <https://www.physi.uni-heidelberg.de/Einrichtungen/FP/anleitungen/F96.pdf> (cited on pages 17, 28).
- [26] Anaïs Schaeffer. *LS2 Report: A new schedule*. June 2020. URL: <https://home.cern/news/news/accelerators/ls2-report-new-schedule> (cited on page 18).
- [31] EUDAQ Development Team. *EUDAQ User Manual*. Oct. 2016. URL: http://eudaq.github.io/manual/EUDAQUserManual_v1.pdf (cited on page 25).

- [34] Danping Zou. *Lecture 04- Projective Geometry*. URL: http://drone.sjtu.edu.cn/dpzou/teaching/course/lecture04-projective_geometry.pdf (cited on page 32).
- [36] V. Blobel. *Software alignment for tracking detectors*. 2006. URL: https://www.desy.de/~sschmitt/blobel/blobel_align.pdf (cited on page 39).
- [37] Giulio Eulisse. *ALICE Analysis Tutorial*. Jan. 2021. URL: <https://alice-doc.github.io/alice-analysis-tutorial/analysis/figures/pid.png> (cited on page 52).

List of Figures

1	Standard Model of particle physics	4
2	The ALICE detector system	5
3	Space-time evolution of the QGP	7
4	Stopping power of muons / Straggling functions in silicon	11
5	Secondary cosmic ray production in Earth's atmosphere	13
6	Vertical fluxes of cosmic rays in the atmosphere	14
7	Energy band structure of different types of solids	15
8	Silicon doping example with phosphorus (n-type) and boron (p-type)	16
9	Schematic of a hybrid- and a monolithic active pixel sensor	17
10	A cross section of the a MAPS pixel	19
11	Threshold scan of a single pixel / Threshold distribution of a plane	20
12	Charge thresholds as a function of DAC parameters / Sensor efficiency	21
13	Noise occupancy	22
14	The ALPIDE telescope / ALPIDE sensor / Telescope case	23
15	In-pixel circuitry	24
16	In-pixel circuitry response / Signal shape / Strobe and trigger signal	24
17	Tracks with gap / Number of gaps per plane	27
18	Cluster shape examples	28
19	Cluster sizes for all events with four or more planes	29
20	Alignment comparison between testbeams during 2019 and 2020	30
21	Calculation of residuals	31
22	Cosmic muon track examples	33
23	χ^2 -distribution before alignment	33
24	Non-associated firing of pixels	34
25	Residuals before alignment	36
26	Residuals after alignment	37
27	χ^2 -distribution after alignment	38
28	Plane position as a function of alignment iterations	38
29	Telescope shearing	39
30	Toy detector alignment approaches	40
31	χ^2 -distribution before and after alignment with fixed-plane approach	40
32	Plane position as a function of alignment iterations (fixed-plane approach)	41
33	χ^2 -distribution after 80 alignment iterations	42
34	Comparison of the alignment approaches	43
35	Comparison of the alignment approaches (unscaled)	43

36	Contaminated event with χ^2_ν value of 24430	52
37	Energy loss in the TPC	52
38	Alignment - alternative initial conditions	53

List of Tables

1	Thresholds of all planes	25
2	Estimated muon rates	26
3	Plane position before and after residual correction	35
4	Plane position after alignment with fixed-plane approach	42

Additional Figures

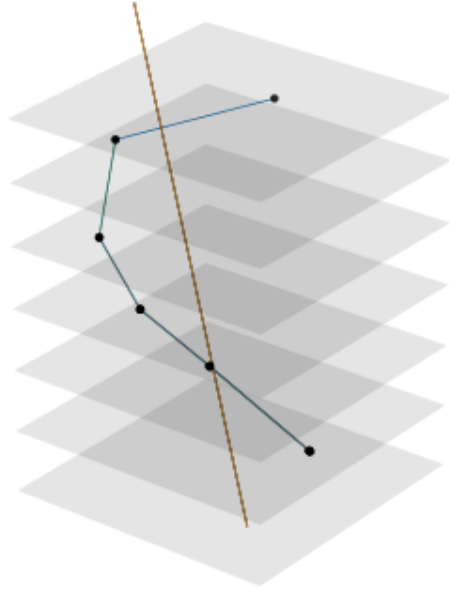


Figure 36: Contaminated event with χ^2_ν value of 24430

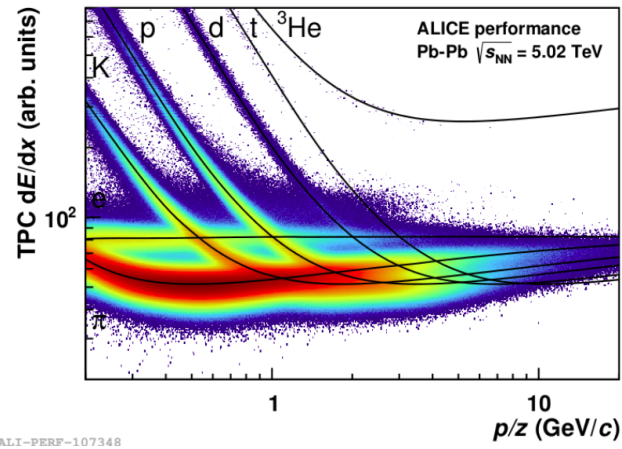


Figure 37: Energy loss as a function of particle momentum measured with the ALICE TPC [37]. The electron line overlaps with the other hadrons, which causes ambiguities.

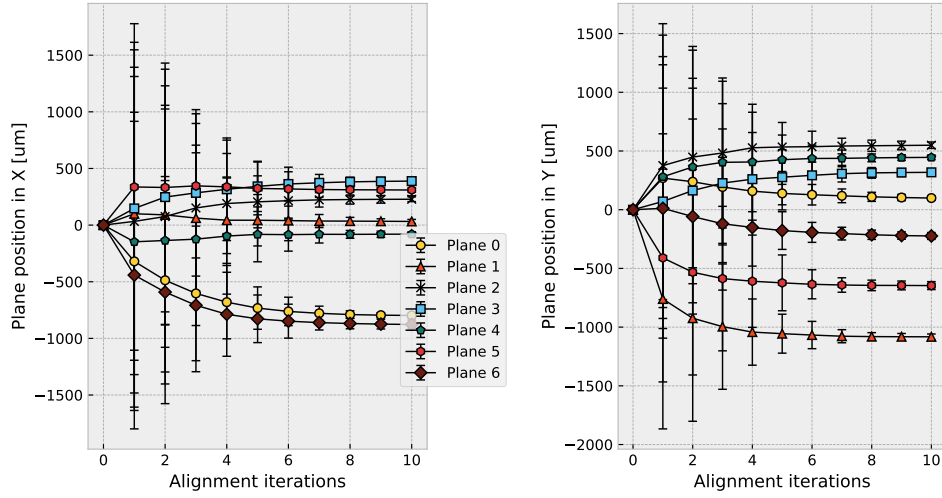


Figure 38: Alignment by the free approach, without first initializing the alignment with the help of testbeam data. The convergence is still much quicker than it is for the fixed-plane approach. However, the initial conditions add a strong virtual shearing to the alignment, as the algorithm converges to seemingly completely different values of the sensor position.

A.6 Neutrino Interaction

(A.6) Different sources claim that the neutrino interaction cross section for neutrinos with energies from 1 MeV to 1 GeV is at most $\sigma = 5.6 \cdot 10^{-38}$ cm. Assuming an average density of $\rho = 5.5$ g/cm³ and an average atomic number of $A = 56$, one can calculate the mean free path

$$\lambda = \frac{1}{\sigma \cdot n_t} = \frac{A}{\sigma \cdot \rho \cdot N_A} = 3.01 \cdot 10^{12} \text{ m}$$

of neutrinos traversing Earth, with N_a being the Avogadro Number and n_t the nuclear density of Earth. Divided by Earth's diameter $d_E = 1.2 \cdot 10^7$ m this yields one neutrino interaction in an average of 250 833 Earths.

Acknowledgement

I would like to express my gratitude to Silvia Masciocchi, who gave me the incredible opportunity to join the ALICE group at GSI and work first hand on one the same type of detectors, which are implemented into the ITS during the currently ongoing upgrade. This has been the most interesting topic for me ever since I enrolled, and her kind supervision and the very helpful discussions during meetings were a great help to guide me through the entire process.

Secondly I would like to thank Bogdan Blidaru for his undying patience, for not only fixing most of the issues that arose during the measurements (of which there were countless), that me and my colleagues were unable to address alone, but also for sticking around even through the hardest of times, may it be helping to correct the thesis itself, or entering the laboratory in a time, where 99% of all access was denied, just to meddle with the NIM-modules. He has been a huge help, aligning all chains of thoughts and reinforcing the structure, that sometimes seemed to waver.

Moreover, i pass many thanks to my colleagues Pascal Becht and David Schledewitz. Apart from your helpful comments and critical questions, that have helped me many times, it was a joy working with you, no matter if in the laboratory, at 3 a.m. in the morning during a testbeam, when something just did not want to work, or even remotely via zoom during these challenging times.

I also have to thank every person, who contributed to this thesis in terms of proofreading and posing helpful comments, who is not mentioned by name.

Finally, i would like to express my deepest gratitude to the closest people in my life for their support. I want to thank Leire Beneitez Vega, who moved in with me and took care of me during the most difficult period of work, ensuring my mental wellbeing wherever she could and handling many tasks around the house. I would like to thank Jan Hubrich, who not only is one of the most faithful people I have ever met in my life, but also constantly reassured me of my abilities and sticking around for hour long work sessions, whenever I felt I needed the company.

Als letztes bedanke ich mich bei meinen Eltern, ohne die Ich jetzt nicht hier in Heidelberg wäre. Ihr habt mir gesagt, dass ich es schaffen kann, und mich immer wieder daran erinnert, auch wenn Ich es selbst oftmals nicht zu glauben vermochte. Ich bedanke mich des Weiteren bei meiner Patentante, die mir mit ihrer Unterstützung viele Sorgen und Last von den Schultern nahm. Du hast immer ein offenes Ohr für meine Probleme gehabt, und bist ein großes Vorbild für mich.

Declaration

I declare that the thesis has been composed by myself and that the work has not be submitted for any other degree or professional qualification. I confirm that the work submitted is my own, except where work which has formed part of jointly-authored publications has been included.

Heidelberg, March 01, 2021

Maurice Donner